CHAPTER TWELVE

Spatial Dynamic Modeling and Analysis

12.1 MODELING AND ANALYSIS TECHNIQUES

Once a sound kinematic model of a spatial system is defined, the remaining ingredients for dynamic analysis include the specification of masses and moments of inertia, initial conditions on position and velocity, and forces that act on the system. A typical sequence in the dynamic analysis of a mechanical system includes the definition of an equilibrium position, inverse dynamic analysis with a kinematically driven system to determine the required driving and reaction forces, and transient dynamic analysis under the influence of applied forces. Examples are analyzed dynamically in this chapter, using the DADS computer code [27], to illustrate the use of the formulation presented in Chapter 11 to support the design of mechanical systems.

12.2 DYNAMIC ANALYSIS OF A SPATIAL SLIDER–CRANK MECHANISM

12.2.1 Model

The spatial slider–crank mechanism shown in Fig. 10.2.1 is used here to demonstrate dynamic analysis. The system configuration and definition of each joint are as presented in the kinematic analysis of Section 10.2. The only additional data required here are the inertia properties of each body, the forces that act, and the initial conditions of motion. The masses and moments of inertia are presented in Table 12.2.1.

TABLE 12.2.1 Inertia Properties of Slider–Crank Components

Body		Mass	$I_{x'x'}$	$I_{y'y'}$	$I_{z'z'}$	$I_{x'y'}$	$I_{y'z'}$	$I_{z'x'}$
Crank	①	0.12	0.0001	0.00001	0.0001	0.0	0.0	0.0
Connecting rod	②	0.5	0.004	0.0004	0.004	0.0	0.0	0.0
Slider	③	2.0	0.0001	0.0001	0.0001	0.0	0.0	0.0
Ground	④	1.0	1.0	1.0	1.0	0.0	0.0	0.0

12.2.2 Inverse Dynamic Analysis

The crank is first required to rotate at a constant angular velocity of 2π rad/s (60 rpm). Torques required at the crank to achieve motion of the system that is dictated by this driver are analyzed. Figure 12.2.1 shows three driving torque curves for connecting rod lengths of $\ell = 0.3$, 0.27, and 0.24 m. At about $t = 0.1$ s, when the slider velocity changes direction, sudden changes in driving torque occur. Note that the variation in torque is most severe for the near singular case

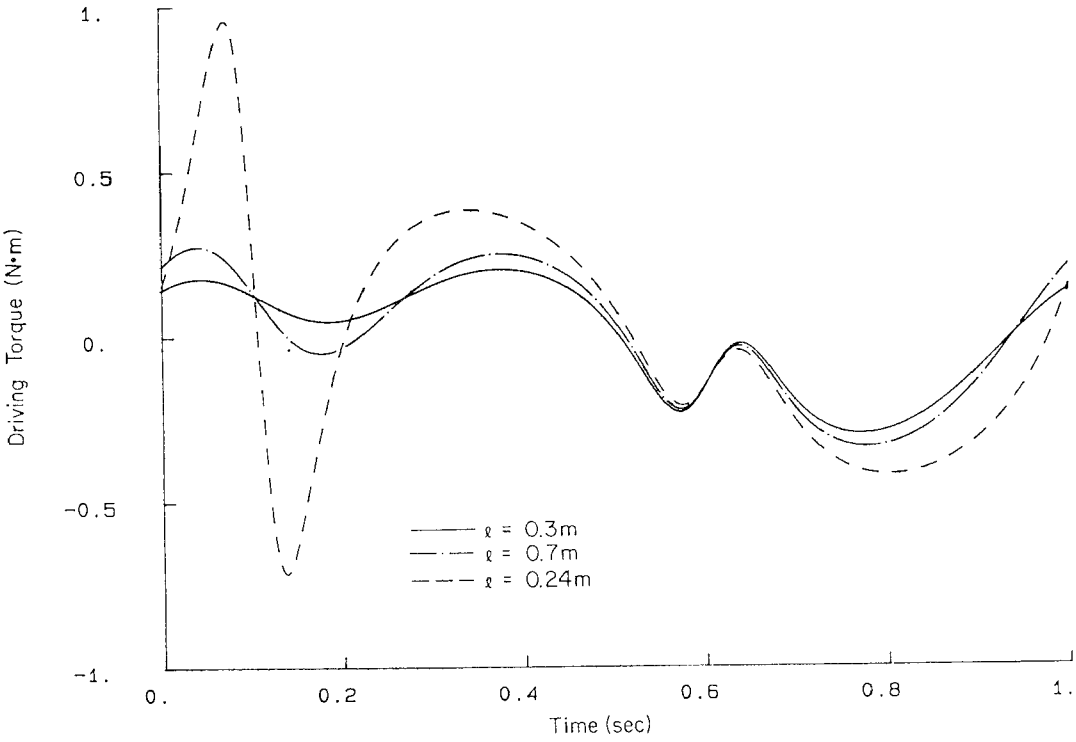

Figure 12.2.1 Driving torque for a spatial slider–crank mechanism.

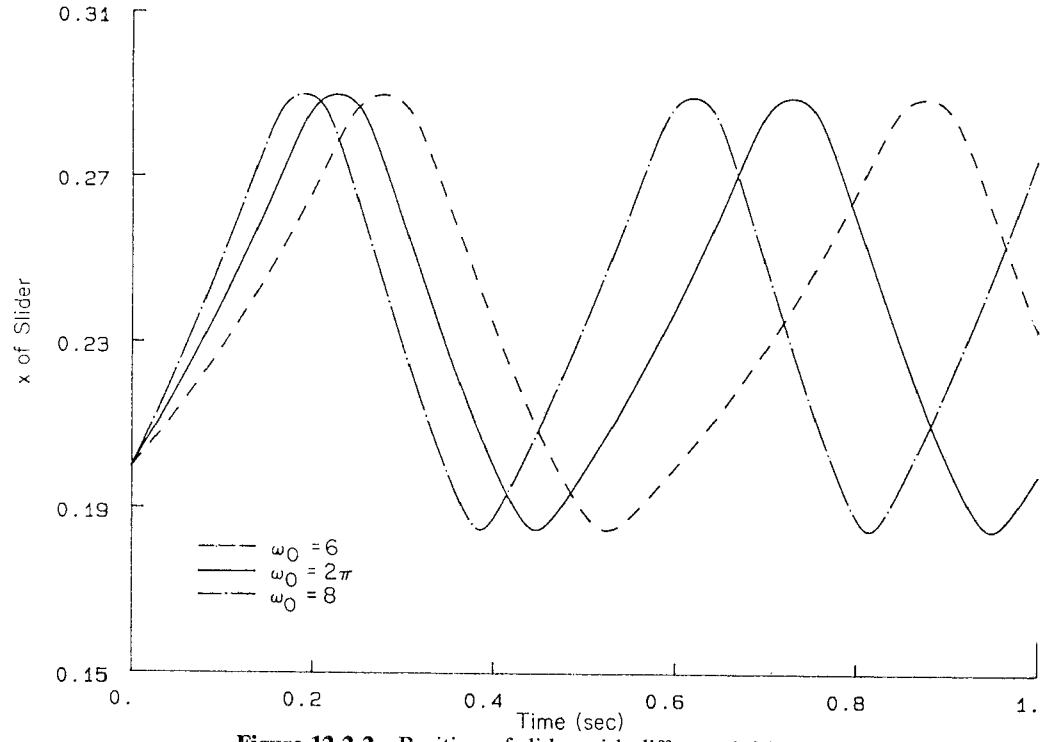

Figure 12.2.2 Position of slider with different initial crank speeds.

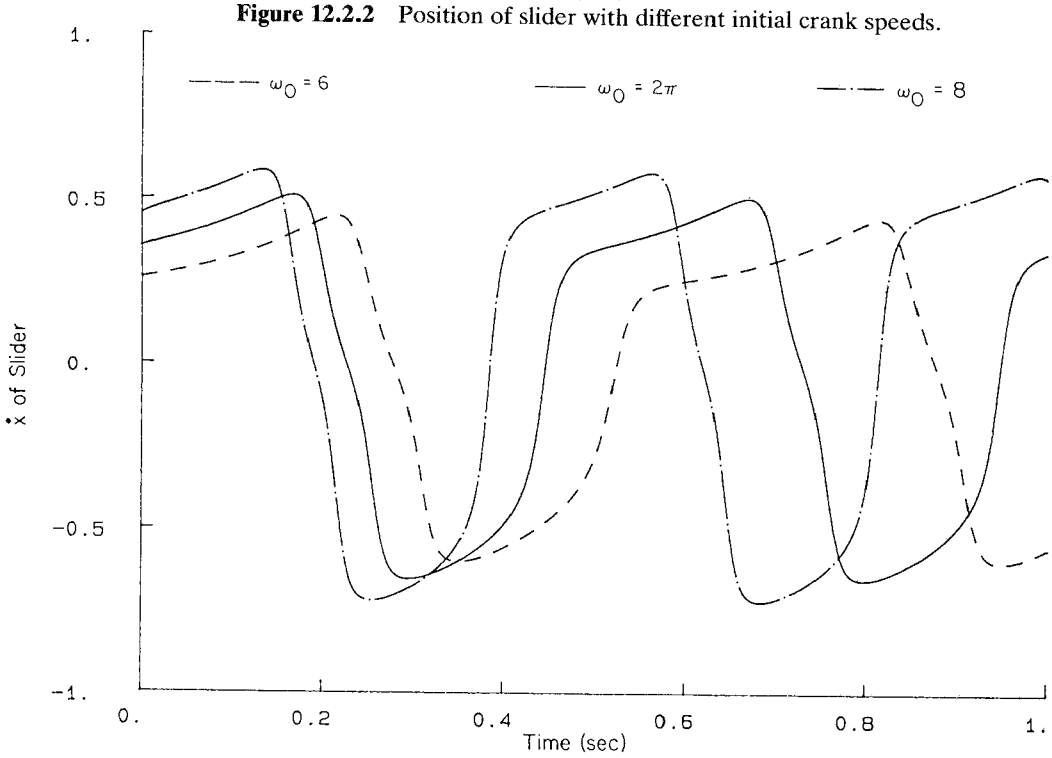

Figure 12.2.3 Velocities of slider with different initial crank speeds.

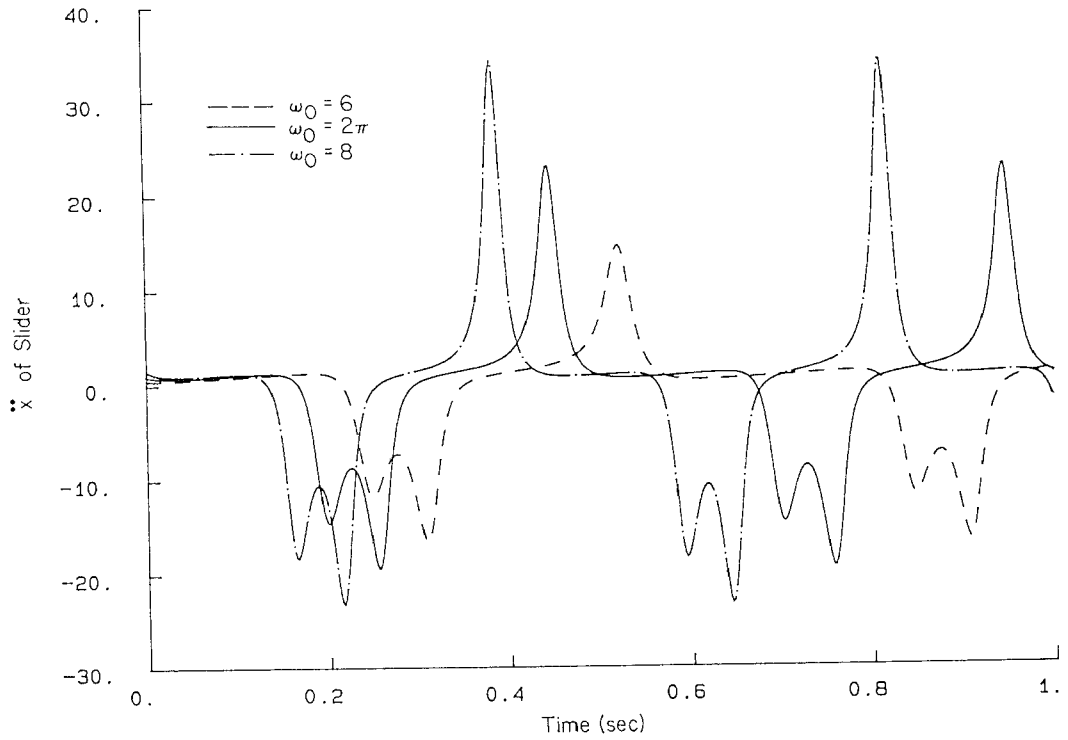

Figure 12.2.4 Accelerations of slider with different initial crank speeds.

$\ell = 0.24$ m, when the slider changes its direction near the plane in which the crank rotates (i.e., near $t = 0.1$ s).

12.2.3 Dynamic Analysis

Three dynamic runs are executed for the nominal design ($\ell = 0.3$ m), with three different initial angular velocities of the crank, $\omega_0 = 6$ rad/s (43.6 rpm), 2π rad/s (60 rpm), and 8 rad/s (76.4 rpm). Plots of positions, velocities, and accelerations of the slider are shown in Figs. 12.2.2 to 12.2.4. Since the system is conservative, plots are periodic, with different periods according to the initial angular velocities.

12.3 DYNAMIC ANALYSIS OF A SPATIAL FOUR-BAR MECHANISM

12.3.1 Alternative Models

The kinematic models of the four-bar mechanism used here are the same as those used in Section 10.3.1 for kinematic analysis. Model 1 in Fig. 10.3.1 consists of

TABLE 12.3.1 Inertia Properties of Four-Bar Mechanism, Model 1

Body	Mass	$I_{x'x'}$	$I_{y'y'}$	$I_{z'z'}$	$I_{x'y'}$	$I_{y'z'}$	$I_{z'x'}$
Link ①	2.0	4.0	2.0	0.0	0.0	0.0	0.0
Link ②	1.0	12.4	0.01	0.0	0.0	0.0	0.0
Link ③	1.0	4.54	0.01	0.0	0.0	0.0	0.0
Ground	1.0	1.0	1.0	1.0	0.0	0.0	0.0

four bodies (including ground) and uses universal and spherical joints. Model 2 in Fig. 10.3.2 consists of three bodies and uses a spherical–spherical composite joint.

The masses and moments of inertia of the components of model 1 are presented in Table 12.3.1. Properties for the bodies that make up model 2 are obtained by simply ignoring link 2 in Table 12.3.1.

12.3.2 Equilibrium Analysis

Gravity is taken as acting in the negative z direction. If gravitational force is the only external force acting on the system, it is expected that the equilibrium position of the system will have link 3 rotated to reach lower z coordinates of centroids than the position shown in Fig. 10.3.1 and defined quantitatively in Table 10.3.5. The resulting equilibrium configuration is presented in Table 12.3.2. Note that the z coordinates of links 2 and 3 are near their local minima at point A in Fig. 10.3.4. Since the heights of their centers of mass dominate the total potential energy of the system, the relative minimum point A of link 3 in Fig. 10.3.4, which corresponds to the configuration of Table 12.3.2, is a position of relative minimum total potential energy; that is, it is a stable equilibrium configuration.

Note that the z coordinate of link 3 could reach the global minimum point B of Fig. 10.3.4 if the initial estimate used to start the minimization algorithm had been nearer this configuration. A different equilibrium position would thus have

TABLE 12.3.2 Equilibrium Position of Four-Bar Mechanism, Model 1, under Gravitational Load

Body	x	y	z	e_0	e_1	e_2	e_3
Link ①	0.0	0.0	0.0	0.4722	−0.8815	0.0	0.0
Link ②	0.4281	−3.418	2.238	0.3080	−0.1269	0.9065	−0.2595
Link ③	−1.572	−8.5	2.792	0.2932	−0.6435	0.6435	−0.2932
Ground	0.0	0.0	0.0	1.0	0.0	0.0	0.0

TABLE 12.3.3 Equilibrium Position of Four-Bar Mechanism, Model 2, under Gravitational Load

Body	x	y	z	e_0	e_1	e_2	e_3
Link ①	0.0	0.0	0.0	0.8665	0.4992	0.0	0.0
Link ②	−6.610	−8.5	2.622	0.6530	−0.2713	0.2713	−0.6530
Ground	0.0	0.0	0.0	1.0	0.0	0.0	0.0
Point A	0.0	−1.730	1.003				

been achieved. This is another illustration of the effect of nonlinearities in the kinematics and dynamics of machines, leading to multiple solutions.

For model 2, the resulting equilibrium configuration is given in Table 12.3.3.

12.3.3 Inverse Dynamic Analysis

Inverse dynamic analysis is carried out by imposing a constant angular velocity of link 1, as in Section 10.3.3. Plots of the required driving torque and the x component of the reaction force at revolute joint A are presented in Fig. 12.3.1.

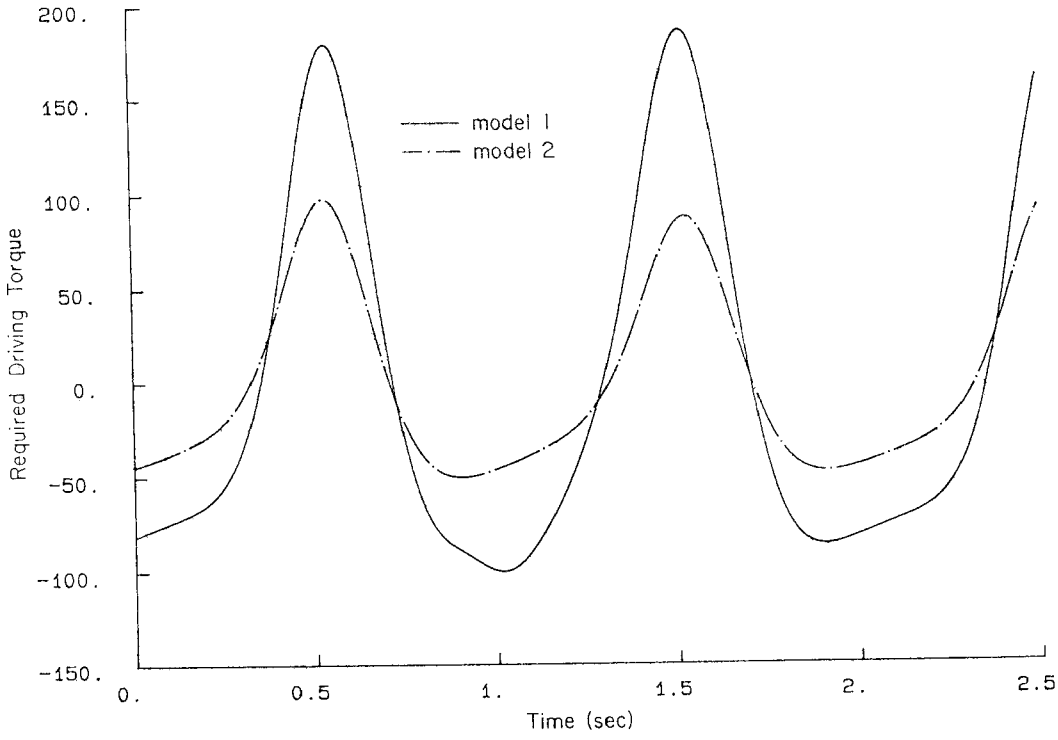

Figure 12.3.1(a) Driving torque at point A.

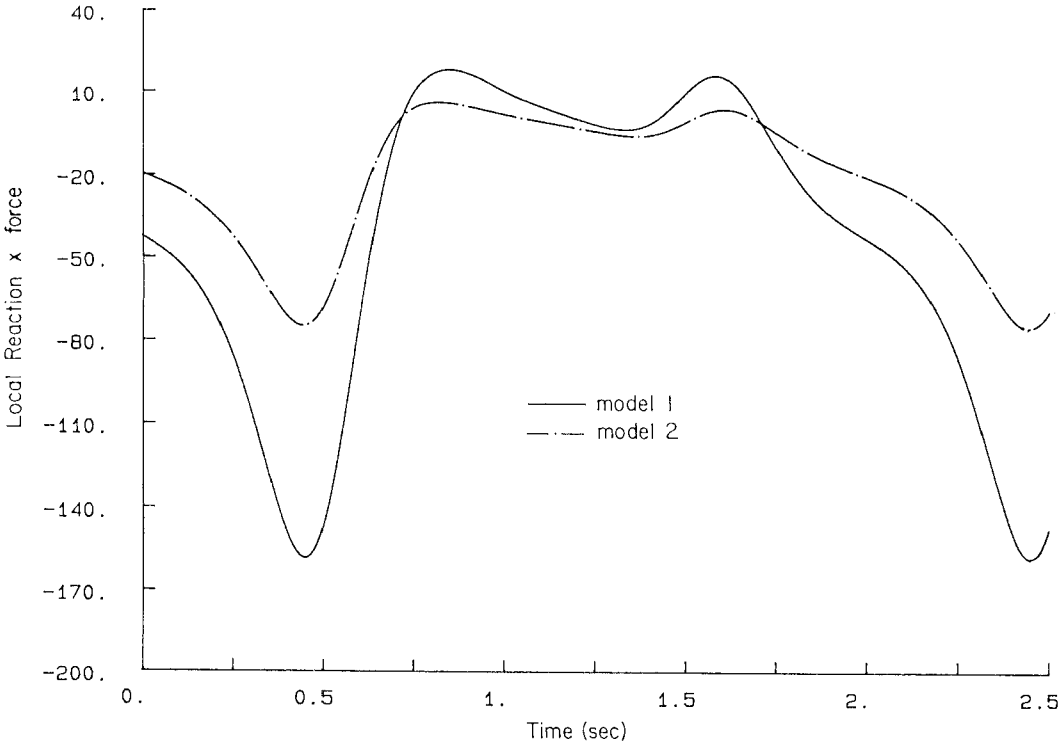

Figure 12.3.1(b) Reaction x force at point A.

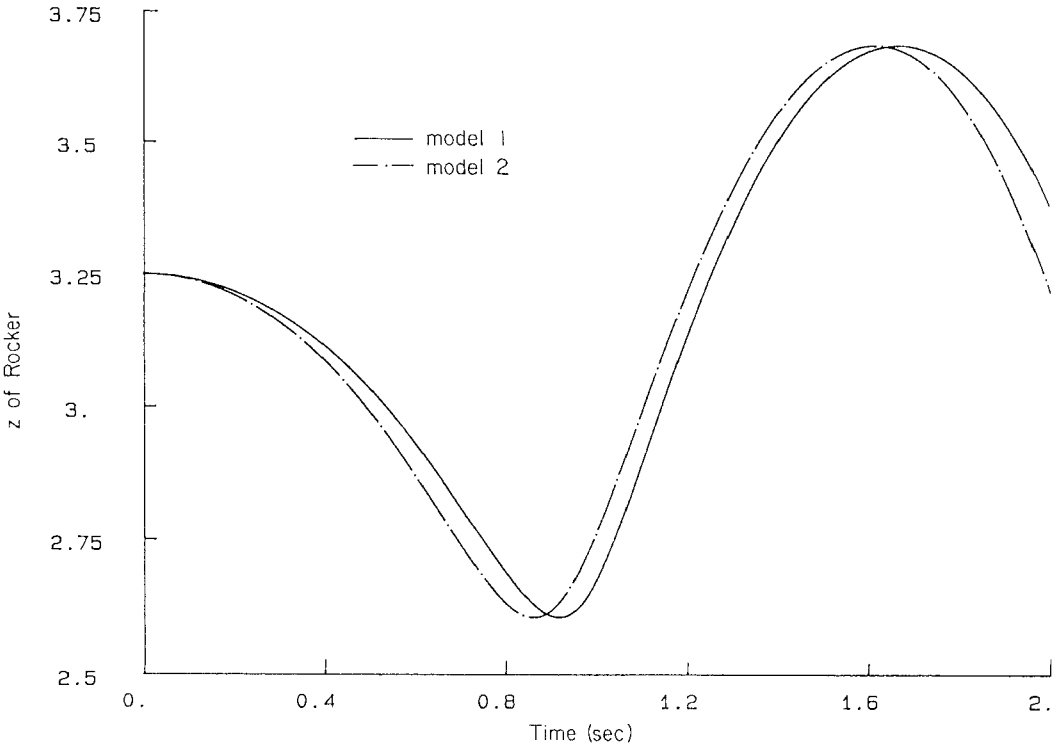

Figure 12.3.2(a) Position of centroid of link CD.

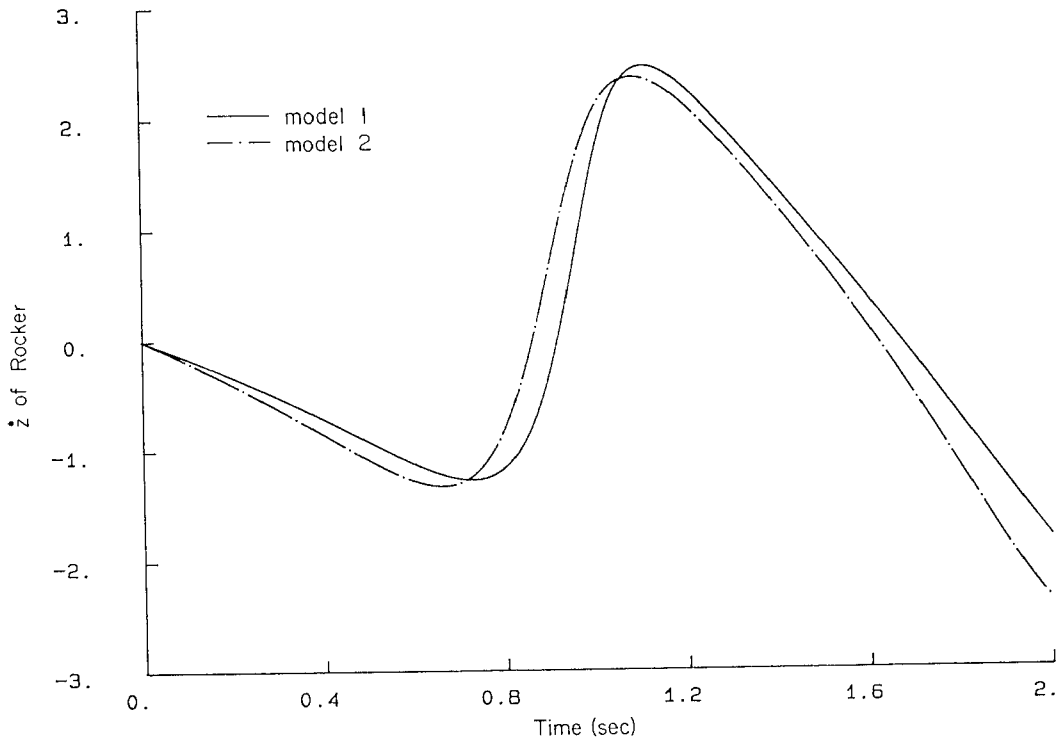

Figure 12.3.2(b) Velocity of centroid of link *CD*.

Note that, due to different inertia properties, the required driving torques and reaction forces in models 1 and 2 are different.

12.3.4 Dynamic Analysis

Dynamic response of the spatial four-bar mechanism is analyzed by imposing a counterclockwise torque $n = 10\,\mathrm{N}\cdot\mathrm{m}$ on link 1. With the same initial position shown in Fig. 10.3.1 (Table 10.3.5), the system is started from rest. Plots of the position and velocity of the centroid of link *CD* (link 3 in model 1 and link 2 in model 2) are given in Fig. 12.3.2. Because the inertia properties of link *BC* are ignored in model 2, different dynamic response is obtained. Note that the basic character of motion is the same, but the response of model 2 is faster due to its lower inertia.

12.4 DYNAMIC ANALYSIS OF AN AIR COMPRESSOR

12.4.1 Model

Dynamic analysis of the air compressor shown in Fig. 10.4.1 is now carried out. The system configuration and definition of each joint are given in Section 10.4.

TABLE 12.4.1 Inertia Properties of Air Compressor

Body		Mass	$I_{x'x'}$	$I_{y'y'}$	$I_{z'z'}$	$I_{x'y'}$	$I_{y'z'}$	$I_{z'x'}$
Ground	①	1.0	1.0	1.0	1.0	0.0	0.0	0.0
Rotor	②	10.0	0.1	0.01	0.1	0.0	0.0	0.0
Disk	③	2.0	0.04	0.08	0.04	0.0	0.0	0.0
Piston 1	④	1.5	0.002	0.002	0.002	0.0	0.0	0.0
Piston 2	⑤	1.5	0.002	0.002	0.002	0.0	0.0	0.0
Piston 3	⑥	1.5	0.002	0.002	0.002	0.0	0.0	0.0
Piston 4	⑦	1.5	0.002	0.002	0.002	0.0	0.0	0.0
Piston 5	⑧	1.5	0.002	0.002	0.002	0.0	0.0	0.0
Piston 6	⑨	1.5	0.002	0.002	0.002	0.0	0.0	0.0

The only additional data required are the inertia properties of each body, the initial conditions of motion for the system, and the forces that act. The masses and moments of inertia are presented in Table 12.4.1.

To simulate the air pressure that acts on each piston, a force curve characteristic is chosen, as shown in Fig. 12.4.1. The distance A-B is the full stroke of the piston. The valve opens when the pressure is at its maximum, at point C. Dimensions A, B, and C are chosen such that the compression ratio is

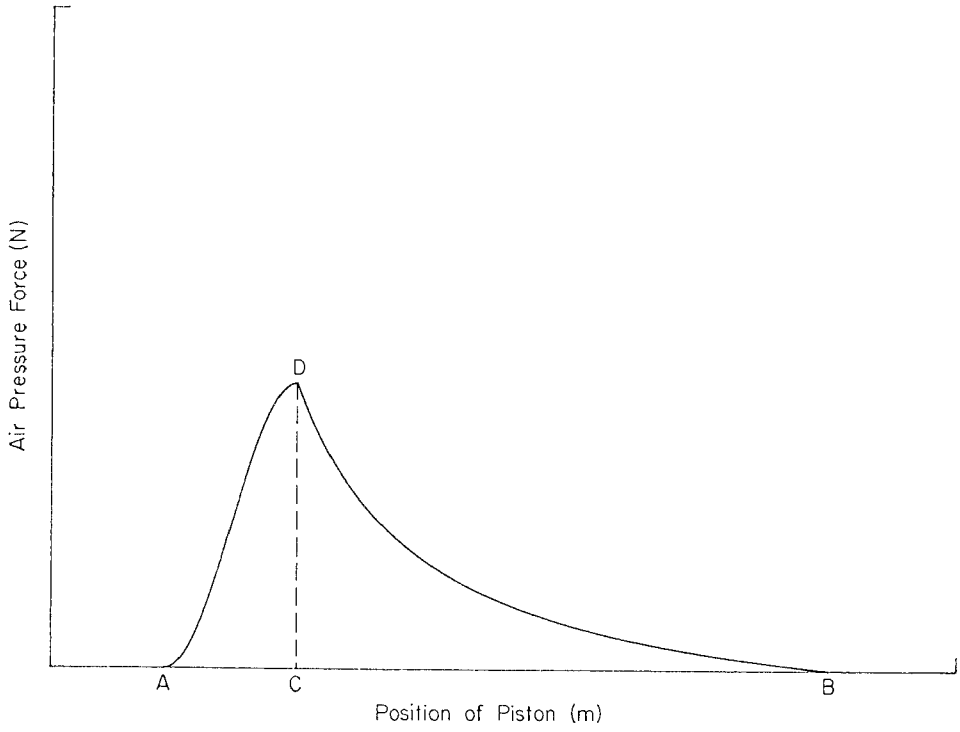

Figure 12.4.1 Air pressure force characterisitic.

5:1. For the nominal tilt angle of 30° for the plate, the stroke AB is 0.2 m. Hence, $AC = 0.04$ m. Force curve DB in Fig. 12.4.1 is

$$F_{DB} = \frac{F_{\max}}{y - y_A} - F_{\min}$$

where y is piston position, y_A is piston position at A (left end of stroke), $F_{\max}$ is the area of piston (m^2) × maximum pressure (N/m^2), and $F_{\min}$ is the force due to air pressure at the right end of the stroke B, which is subtracted to make the gauge pressure zero at B. For this model, $y_A = -1.1$ m, $y_B = -0.9$ m, and the piston bore diameter is 0.1 m.

Force curve AD in Fig. 12.4.1 is

$$F_{AD} = -\frac{F_C}{2}\cos\frac{\pi}{y_C - y_A}(y - y_A) + \frac{F_C}{2}$$

where F_C is force due to air pressure at C and y_C is piston position at C.

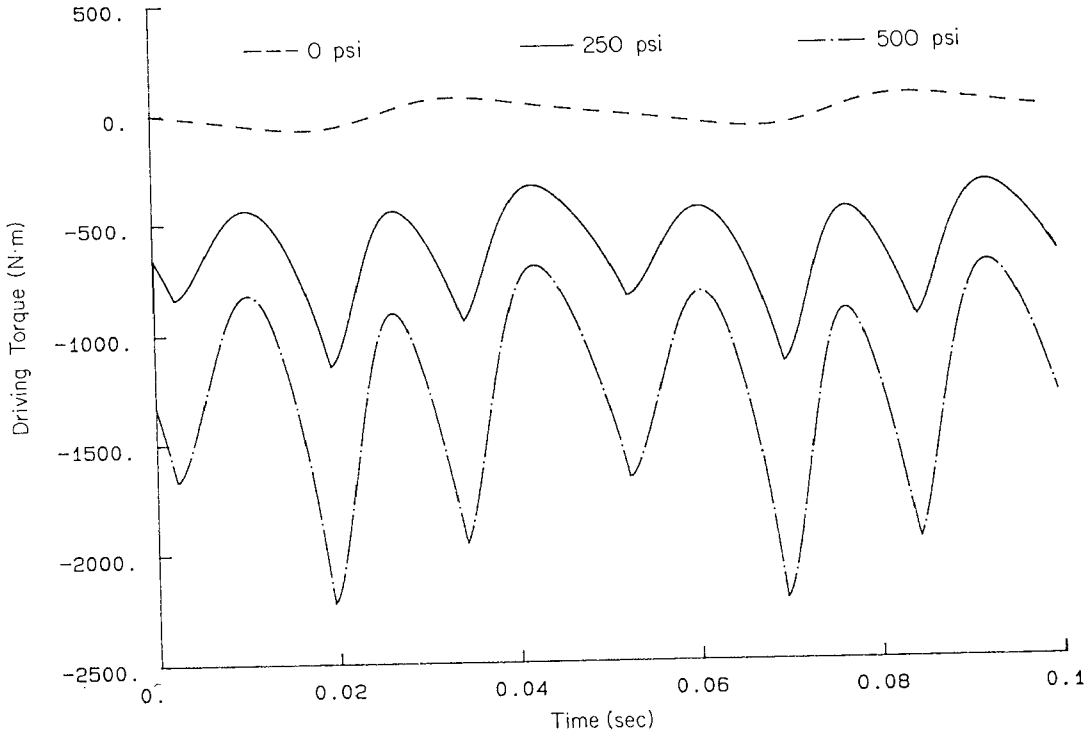

Figure 12.4.2 Driving torque, tilt angle 30°.

12.4.2 Inverse Dynamic Analysis

The rotor is required to rotate at a constant angular velocity of 20π rad/s (600 rpm). To achieve the motion of the system that is dictated by this driver, the torques required at the rotor are analyzed. Figure 12.4.2 shows three driving torque curves, with maximum air pressures of 500, 250, and 0 psi. The x position constraint force shown in Fig. 12.4.3 is essential information for the design of the ball–socket–slider mechanism that prevents the disk from rotating.

Similar analyses are carried out and plotted in Figs. 12.4.4 and 12.4.5, with a tilt angle of the disk of 40°.

12.4.3 Dynamic Analysis

Dynamic simulations are carried out with a constant torque applied to the rotor of the compressor, simulating an external power source such as an electric motor. The constant torque is calculated by integrating the force curve in Fig. 12.4.1, dividing by 2π (one full revolution), and multiplying by 6. Runs are made with three different initial rotor angular velocities of 60 rad/s (573 rpm), 70 rad/s (668 rpm), and 80 rad/s (764 rpm).

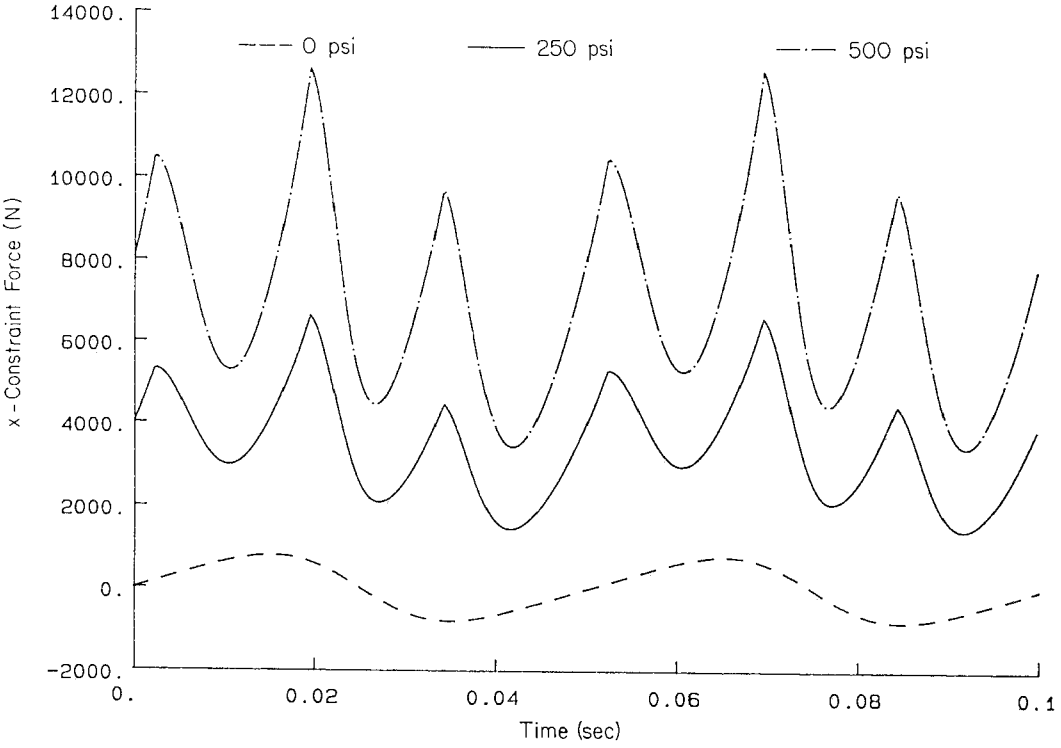

Figure 12.4.3 x position constraint force, tilt angle 30°.

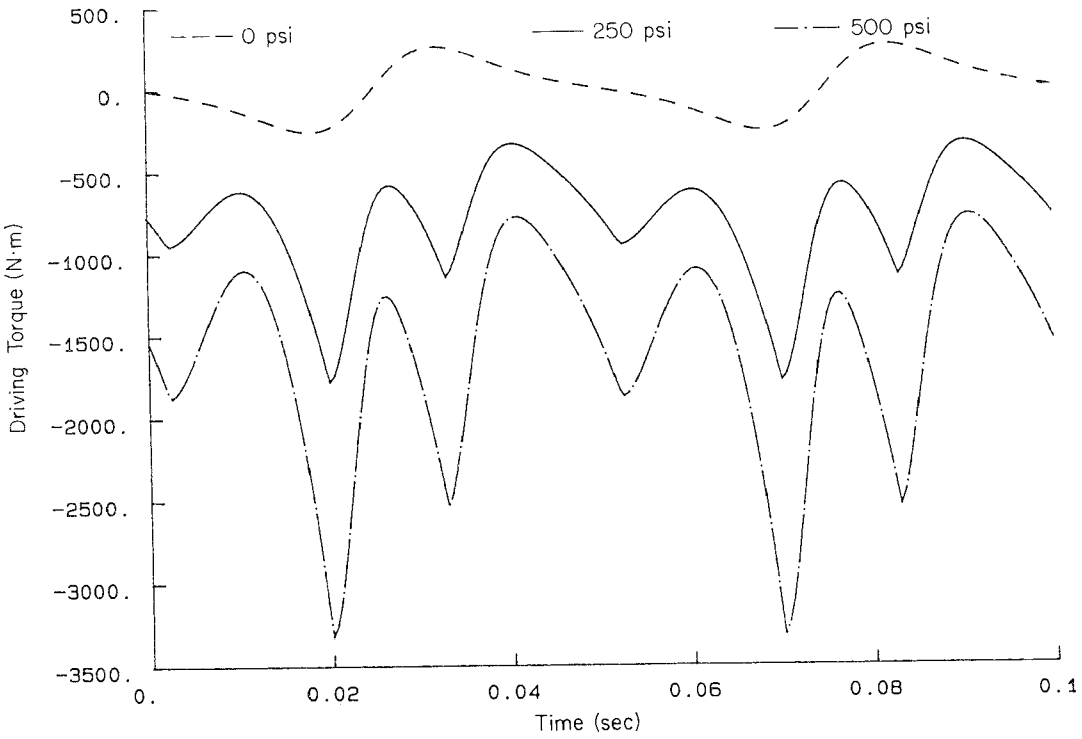

Figure 12.4.4 Driving torque, tilt angle 40°.

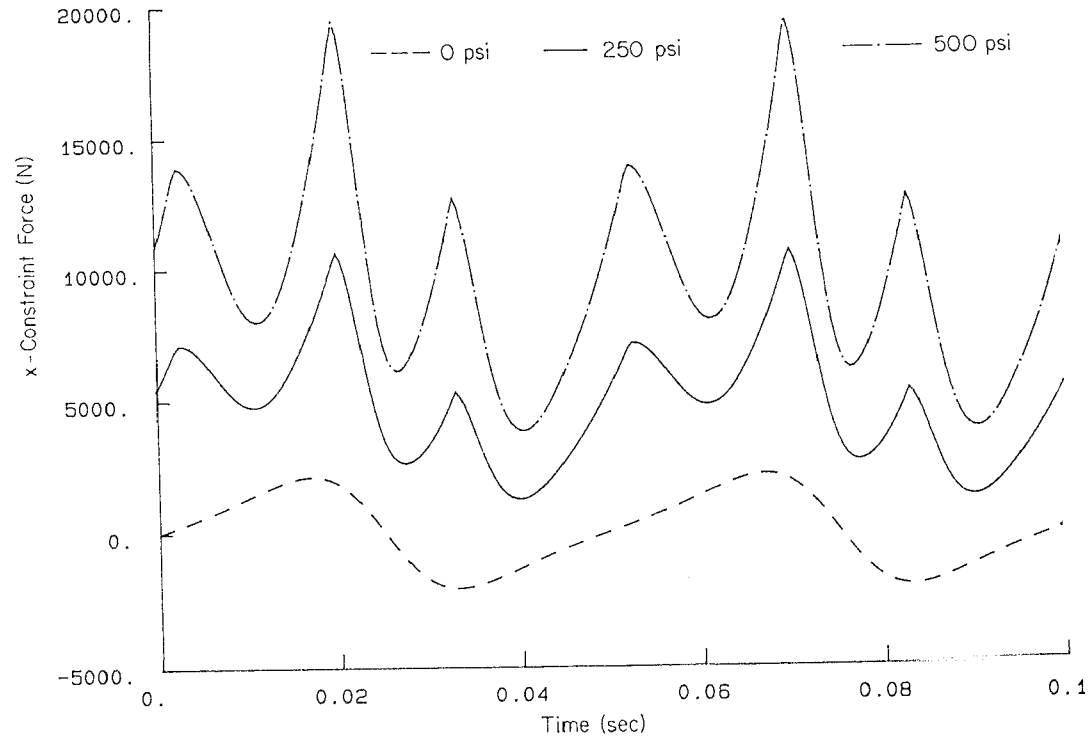

Figure 12.4.5 x position constraint force, tilt angle 40°.

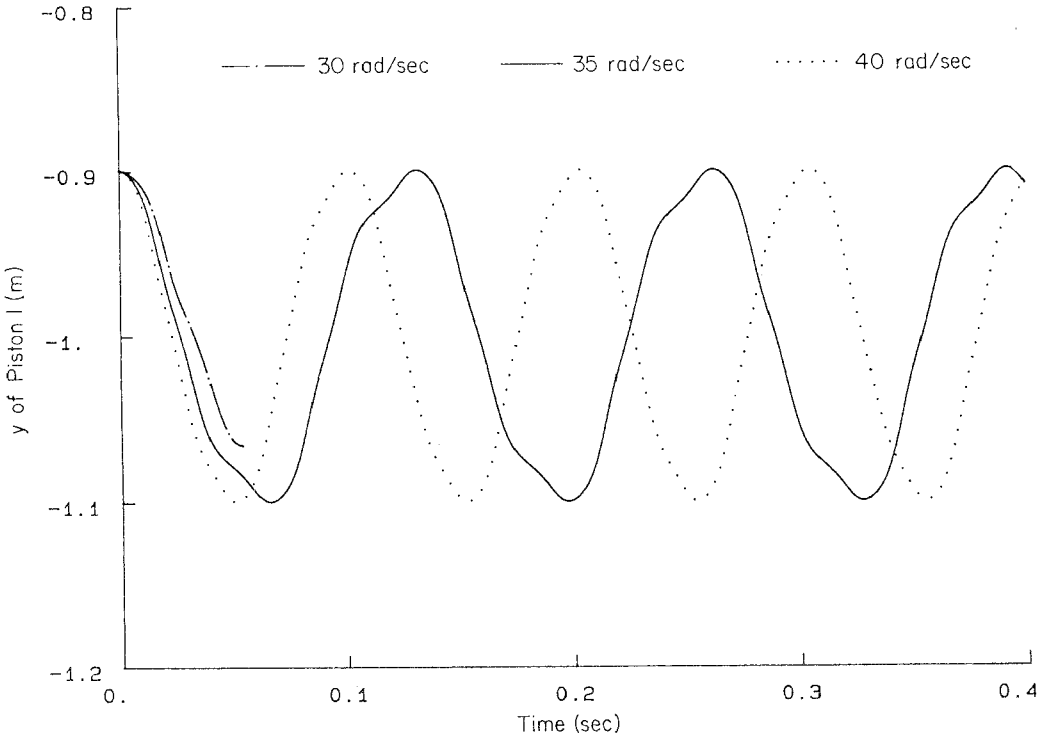

Figure 12.4.6 Position of piston 1 with different initial rotor speeds.

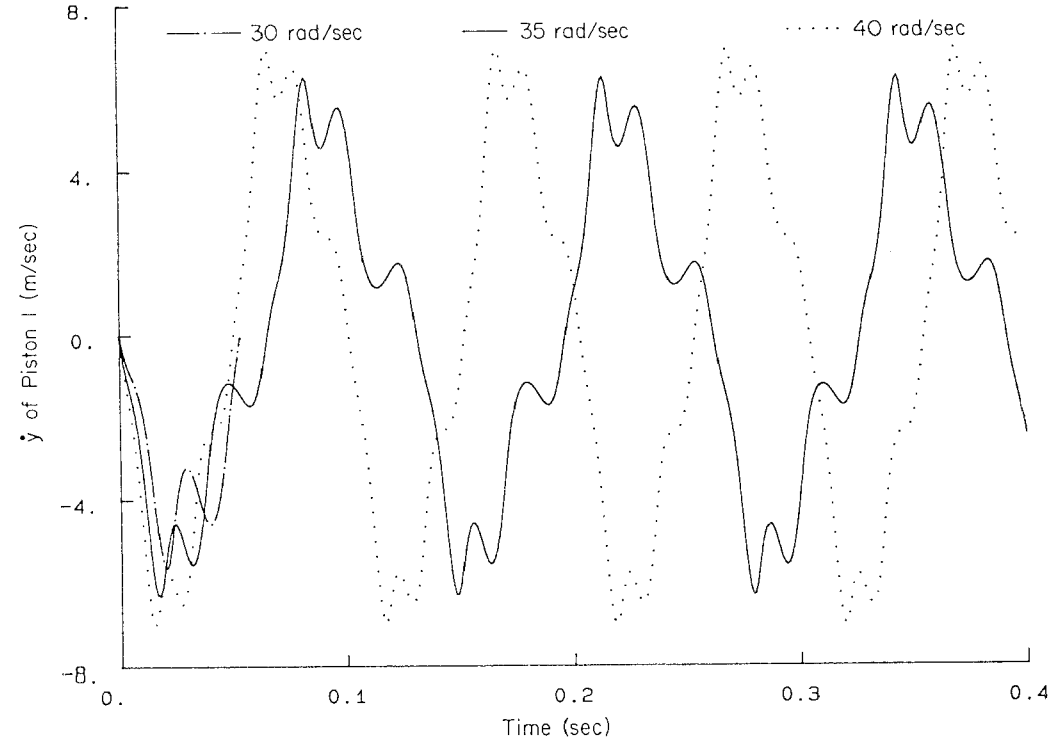

Figure 12.4.7 Velocities of piston 1 with different initial rotor speeds.

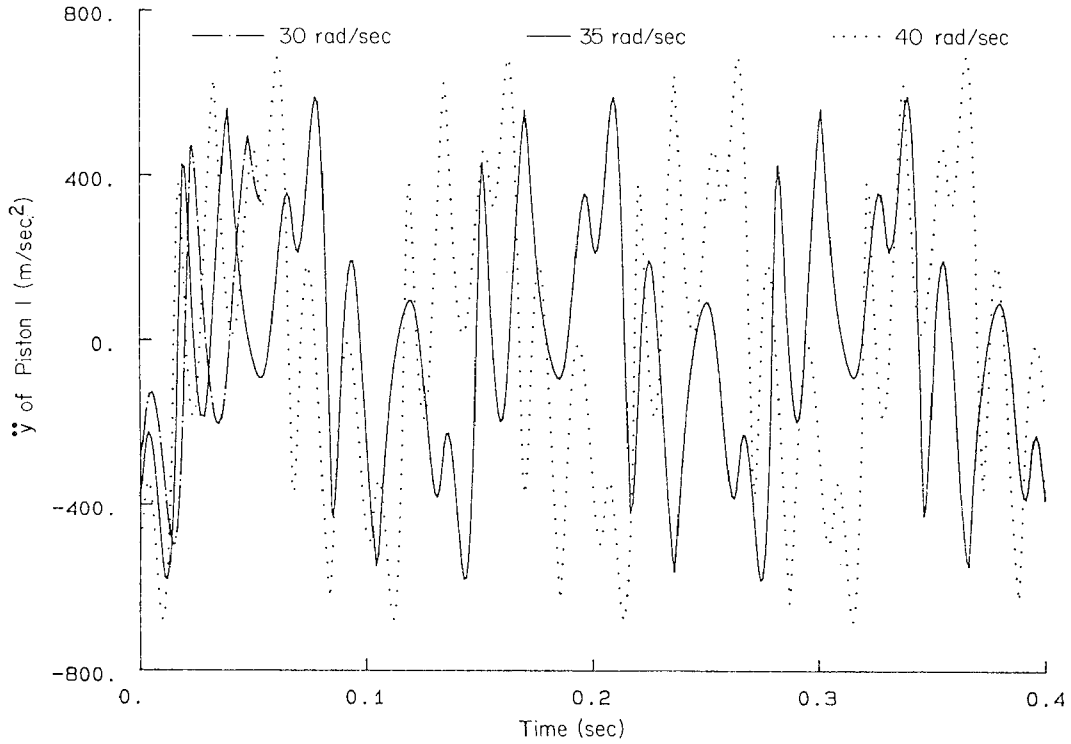

Figure 12.4.8 Accelerations of piston 1 with different initial rotor speeds.

The constant torque is selected to overcome the energy loss in one cycle of the rotor due to the external air pressure force. Therefore, if the initial angular velocity ω_0, and hence the kinetic energy of the system, is not sufficient, motion may stop before one full cycle is completed, as shown for $\omega_0 = 30$ rad/s in Fig. 12.4.6. If the initial angular velocity ω_0, and hence the kinetic energy, is sufficient, then the applied torque yields periodic motion, as shown in Fig. 12.4.6. Plots of the velocities and accelerations of piston 1 are shown in Figs. 12.4.7 and 12.4.8, respectively.

12.5 DYNAMICS OF A VEHICLE

One of the most significant applications of the modeling and analysis of dynamic systems is vehicle system analysis. This section studies the modeling and analysis of the passenger car of Fig. 1.1.10. The objective of this analysis is to predict the motion of the vehicle in response to steering input.

12.5.1 Alternative Models

Two dynamic models of the automobile are created for analysis. Model 1 is composed of bodies 1 through 6 in Fig. 12.5.1, with the front suspension of Fig. 12.5.2. Body 1 is the chassis, bodies 2 to 5 are front and rear wheel assemblies, and body 6 is a steering rack. Model 2 adds a pair of roll-stabilizing bars (bodies 7 and 8) to model 1. The torsional compliance of these bars is modeled by translational springs between their ends and the suspension lower control arms. Masses and moments of inertia of the eight bodies are defined in Table 12.5.1. Products of inertia are all zero.

Each front wheel assembly includes a McPherson strut, whose kinematic connections with the chassis and steering rack are shown in Figs. 12.5.1 and 12.5.2. Each wheel assembly is connected to the chassis by a strut joint at the top (*B*-*C* in Fig. 12.5.2) to represent the McPherson strut and a revolute–spherical joint at the bottom (*A*-*B* in Fig. 12.5.2) to represent the lower control arm. Each rear wheel assembly includes a trailing arm that is connected to the chassis by a revolute joint. The lateral position of the steering rack is controlled by a pinion on the steering column. It is connected to the chassis by a translational joint. The tie rods that connect the rack and wheel assemblies are modeled as distance constraints. Roll-stabilizing bars (bodies 7 and 8) are connected to the chassis by revolute joints at points *J* and *K*, respectively.

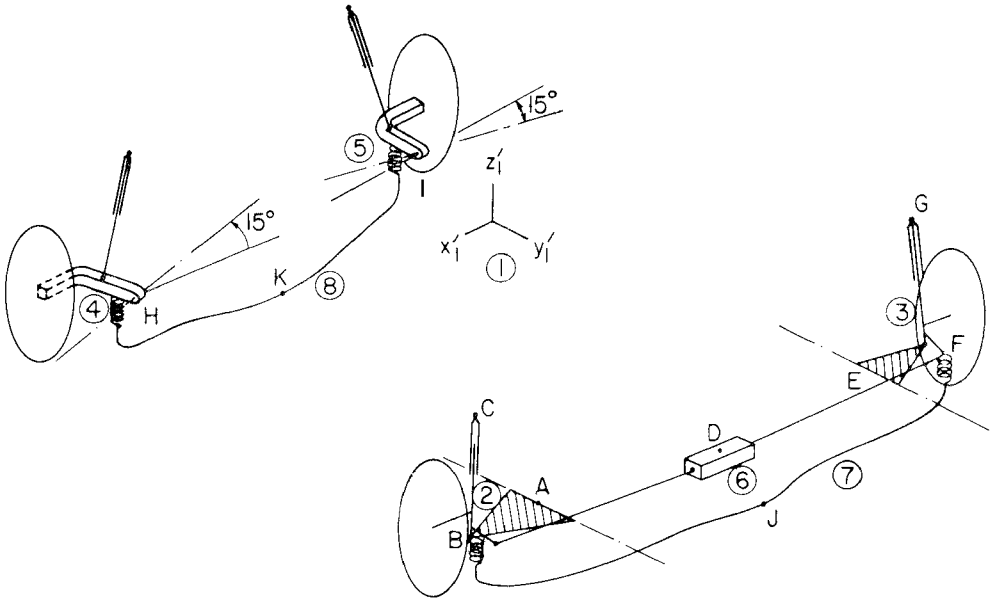

Figure 12.5.1 Automobile suspension schematic.

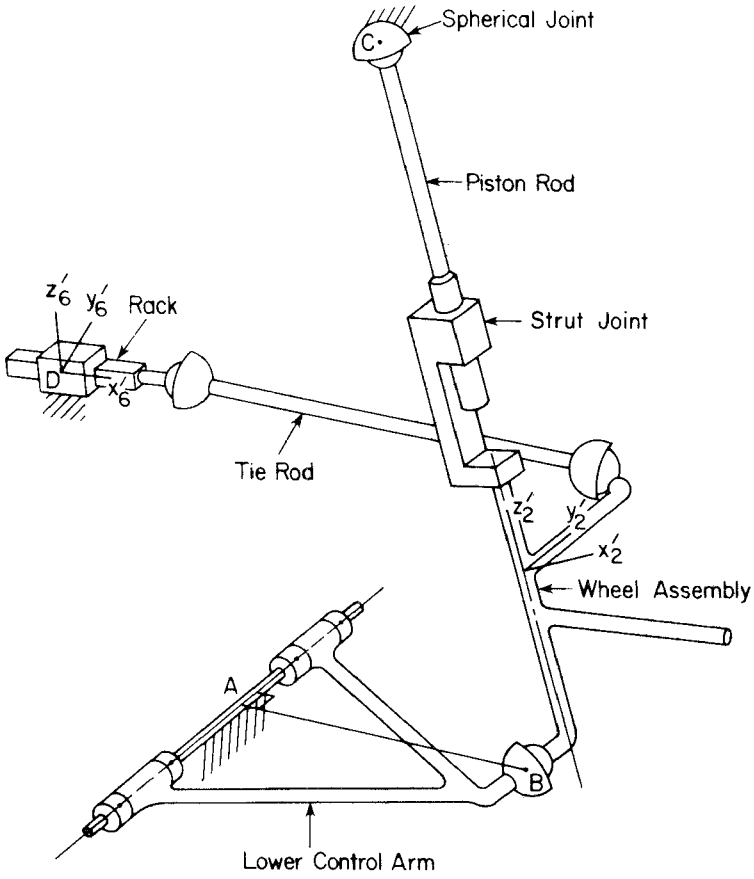

Figure 12.5.2 McPherson strut front suspension.

TABLE 12.5.1 Inertia Properties of the Vehicle

Body		Mass	$I_{x'x'}$	$I_{y'y'}$	$I_{z'z'}$
Chassis	①	1247.5	1240.1	209.6	139.9
Wheel assembly (FR)	②	37.6	1.0	0.5	1.0
Wheel assembly (FL)	③	37.6	1.0	0.5	1.0
Wheel assembly (RR)	④	43.0	0.67	1.5	1.2
Wheel assembly (RL)	⑤	43.0	0.67	1.5	1.2
Rack	⑥	0.1	0.01	0.01	0.01
Stabilizing bar (F)	⑦	1.0	0.1	0.01	0.01
Stabilizing bar (R)	⑧	1.0	0.1	0.01	0.01

The kinematic model of model 2 is described as follows:

Bodies	
Eight bodies	$nc = 56$
Constraints	
Revolute–spherical joint: A-B	2
Strut joint: B-C	2
Translational joint: D	5
Revolute–spherical joint: E-F	2
Strut joint: F-G	2
Revolute joint: H	5
Revolute joint: I	5
Revolute joint: J	5
Revolute joint: K	5
Distance constraint: ②-⑥	1
Distance constraint: ③-⑥	1
Driving constraint: D	1
Euler parameter normalization constraint	8
	$nh = 44$
DOF = 56 − 44 = 12.	

Tables 12.5.2 to 12.5.6 define the kinematic joint definition data for model 2. Eight internal TSDA force elements are used to model the vehicle suspension system, including the roll-stabilizing bars. Table 12.5.7 defines the attachment points and physical characteristics of these elements.

TABLE 12.5.2 Revolute–Spherical Joint Data

Joint *A*-*B*

Body \ Point	*P*			*Q*			*R*		
	x'	y'	z'	x'	y'	z'	x'	y'	z'
Chassis ①	0.33	1.1735	−0.3923	0.322	0.8675	−0.3893	0.33	1.1735	0.0
Wheel assembly ②	0.0507	0.0321	−0.2044	0.0507	0.0321	1.0	0.0507	1.0	−0.2044

Distance = 0.203

Joint *E*-*F*

Body \ Point	*P*			*Q*			*R*		
	x'	y'	z'	x'	y'	z'	x'	y'	z'
Chassis ①	−0.33	1.1735	−0.3923	−0.322	0.8675	−0.3893	−0.33	1.1175	0.0
Wheel assembly ③	−0.0507	0.0321	−0.2044	−0.0507	0.0321	1.0	−0.0507	1.0	−0.2044

Distance = 0.203

TABLE 12.5.3 Strut Joint Data

Joint *B-C*

Body \ Point		*P*			*Q*			*R*	
	x'	y'	z'	x'	y'	z'	x'	y'	z'
Chassis ①	0.5011	1.1162	0.1998	0.5011	1.1162	1.0	0.5011	2.0	0.1998
Wheel assembly ②	0.0	0.0	0.0	1.0	0.0	0.0	0.0	1.0	0.0

Joint *F-G*

Body \ Point		*P*			*Q*			*R*	
	x'	y'	z'	x'	y'	z'	x'	y'	z'
Chassis ①	−0.5011	1.1162	0.1998	−0.5011	1.1162	1.0	−0.5011	2.0	0.1998
Wheel assembly ③	0.0	0.0	0.0	1.0	0.0	0.0	0.0	1.0	0.0

TABLE 12.5.4 Translational Joint Data

Body \ Point		*P*			*Q*			*R*	
	x'	y'	z'	x'	y'	z'	x'	y'	z'
Chassis ①	0.0	1.2675	−0.3748	1.0	1.2675	−0.3748	0.0	2.0	−0.3748
Rack and pinion ⑥	0.0	0.0	0.0	1.0	0.0	0.0	0.0	1.0	0.0

TABLE 12.5.5 Revolute Joint Data

Joint *H*

Body \ Point		*P*			*Q*			*R*	
	x'	y'	z'	x'	y'	z'	x'	y'	z'
Chassis ①	0.2026	−1.0095	−0.285	−0.7633	−1.2683	−0.285	0.2026	−1.0095	0.0
Wheel assembly ④	−0.3774	0.278	0.0093	−1.343	0.0192	0.0093	−0.3774	0.278	0.0

Joint *I*

Body \ Point		*P*			*Q*			*R*	
	x'	y'	z'	x'	y'	z'	x'	y'	z'
Chassis ①	−0.2026	−1.0095	−0.285	0.7633	−1.2683	−0.285	−0.2026	−1.0095	0.0
Wheel assembly ⑤	0.3774	0.278	0.0093	1.343	0.0192	0.0093	0.774	0.278	1.0

Joint *J*

Body \ Point		*P*			*Q*			*R*	
	x'	y'	z'	x'	y'	z'	x'	y'	z'
Chassis ①	0.0	1.061	−0.3263	1.0	1.061	−0.3263	0.0	2.0	−0.3263
Stabilizing bar ⑦	0.0	0.0	0.0	1.0	0.0	0.0	0.0	1.0	0.0

TABLE 12.5.5 continued

		Joint K								
Body \ Point		P			Q			R		
		x'	y'	z'	x'	y'	z'	x'	y'	z'
Chassis	①	0.0	−1.4075	−0.1813	1.0	−1.4075	−0.1813	0.0	2.0	−0.1813
Stabilizing bar	⑧	0.0	0.0	0.0	1.0	0.0	0.0	0.0	1.0	0.0

TABLE 12.5.6 Distance Constraint Data

		Distance ②–⑥								
Body \ Point		P			Q			R		
		x'	y'	z'	x'	y'	z'	x'	y'	z'
Wheel assembly	②	0.07	0.155	−0.186	0.07	0.155	1.0	0.07	1.0	−0.186
Rack and pinion	⑥	0.305	0.0	0.0	0.305	0.0	1.0	0.305	1.0	0.0

Distance = 0.3742

		Distance ③–⑥								
Body \ Point		P			Q			R		
		x'	y'	z'	x'	y'	z'	x'	y'	z'
Wheel assembly	③	−0.07	0.155	−0.186	−0.07	0.155	1.0	−0.07	1.0	−0.186
Rack and pinion	⑥	−0.305	0.0	0.0	−0.305	0.0	1.0	−0.305	1.0	−0.0

Distance = 0.3742.

Tire forces must be considered to complete the vehicle model. Tire vertical force F_{ver} is calculated as

$$F_{ver} = k_t \times d$$

where k_t is the tire spring constant and d is tire vertical deformation, which is

TABLE 12.5.7 TSDA Data

TSDA	P_i	P_j	k	C	L_0
①-②	(0.5011, 1.1162, 0.1998)	(0.0, 0.0, 0.0)	38,600	150	0.4992
①-③	(−0.5011, 1.1162, 0.1998)	(0.0, 0.0, 0.0)	38,600	150	0.4992
①-④	(0.58, −1.2875, 0.2)	(0.0, 0.0, 0.0)	38,600	200	0.5641
①-⑤	(−0.58, −1.2875, 0.2)	(0.0, 0.0, 0.0)	38,600	200	0.5641
⑦-②	(0.509, 0.1405, 0.02)	(−0.0897, 0.0168, −0.2119)	83,400	0	0.1011
⑦-③	(−0.509, 0.1405, 0.02)	(0.0897,0.0168, −0.2119)	83,400	0	0.1011
⑧-④	(0.392, 0.168, −0.0474)	(−0.1832, 0.048, −0.0423)	9,330	0	0.0943
⑧-⑤	(−0.392, 0.168, −0.0474)	(0.1832, 0.048, −0.0423)	9,330	0	0.0943

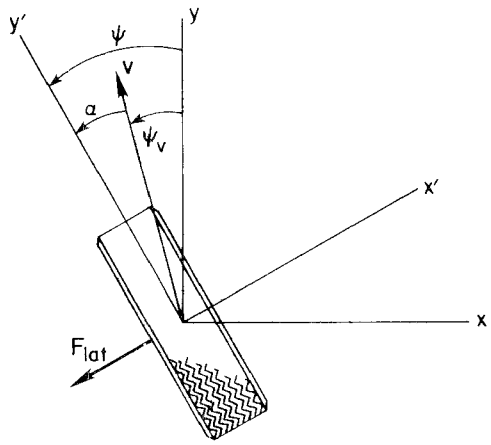

Figure 12.5.3 Tire schematic.

defined by the height of the spindle above the road surface. Tire lateral force F_{lat} is generated by lateral slip of the tire on the road surface and is approximated as

$$F_{\text{lat}} = C_\alpha \times \alpha$$

where C_α is tire cornering stiffness and α is the tire slip angle. This lateral force cannot exceed μF_{ver}, where $\mu < 1$ is the coefficient of friction between the tire and the road surface.

Figure 12.5.3 schematically defines the tire slip angle α, which is the angle between the tire heading and the tire velocity vector $\mathbf{v}$. The tire is assumed to be vertical and the road surface is the global x-y plane. A local x'-y' reference frame is fixed in the spindle to which the wheel is attached. Angles ψ and ψ_v are called the tire yaw (or heading) and velocity angles, respectively, as shown in Fig. 12.5.3. The tire slip angle is thus

$$\alpha = \psi - \psi_v \tag{12.5.1}$$

Angle ψ is calculated from the definition of the Euler parameters of the spindle, presuming the tire is vertical; that is,

$$\cos\frac{\psi}{2} = e_0$$

or

$$\psi = 2\cos^{-1} e_0, \qquad 0 \leq \psi < 2\pi \tag{12.5.2}$$

The tire velocity angle ψ_v is

$$\psi_v = -\tan^{-1}\frac{v_x}{v_y} \tag{12.5.3}$$

TABLE 12.5.8 Position and Orientation Estimates

Body \ GC		x	y	z	e_1	e_2	e_3
Chassis	①	0.0	0.0	0.55	0.0	0.0	0.0
Wheel assembly	②	0.6	1.17	0.34	0.0	0.0	0.0
Wheel assembly	③	−0.6	1.17	0.34	0.0	0.0	0.0
Wheel assembly	④	0.58	−1.29	0.26	0.0	0.0	0.0
Wheel assembly	⑤	0.58	−1.29	0.26	0.0	0.0	0.0
Rack	⑥	0.0	1.26	0.16	0.0	0.0	0.0
Stabilizing bar	⑦	0.0	1.05	0.21	0.0	0.0	0.0
Stabilizing bar	⑧	0.0	−1.40	0.38	0.0	0.0	0.0

12.5.2 Equilibrium Analysis

Static equilibrium analysis of model 1 is performed using dynamic analysis of the vehicle. Estimates of the position and orientation of the vehicle are tabulated in Table 12.5.8. Figures 12.5.4 and 12.5.5 show settling of the vehicle to an equilibrium position due to damping in the suspension system. Table 12.5.9 defines the static equilibrium configuration obtained.

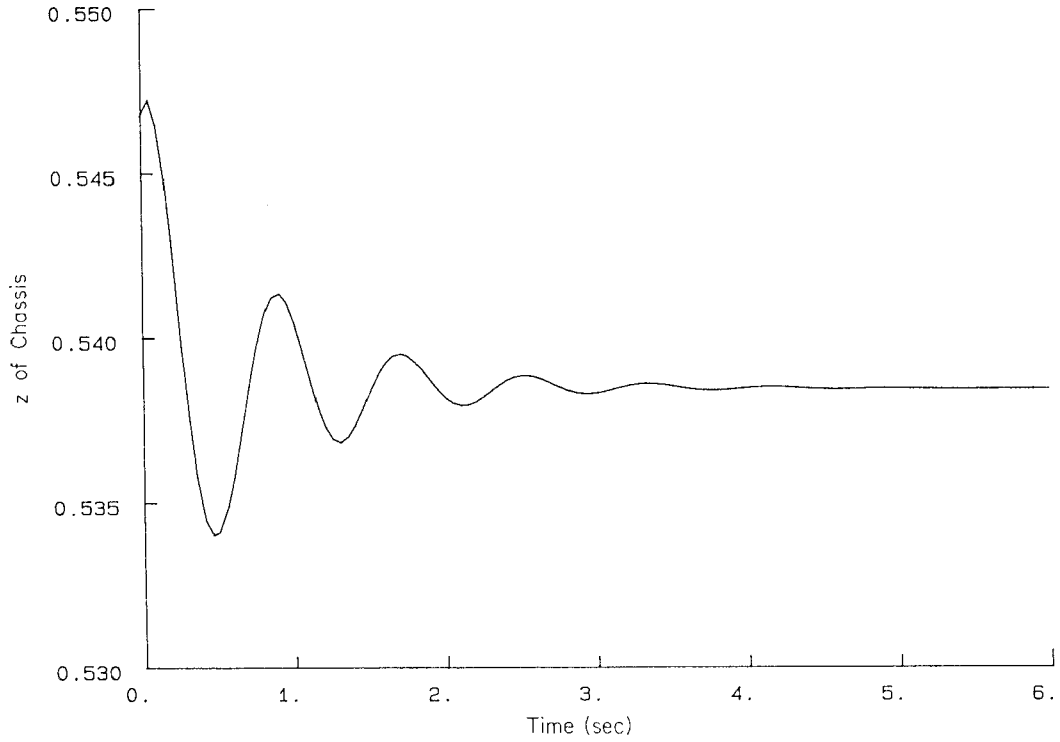

Figure 12.5.4 Vehicle equilibrium height (model 1).

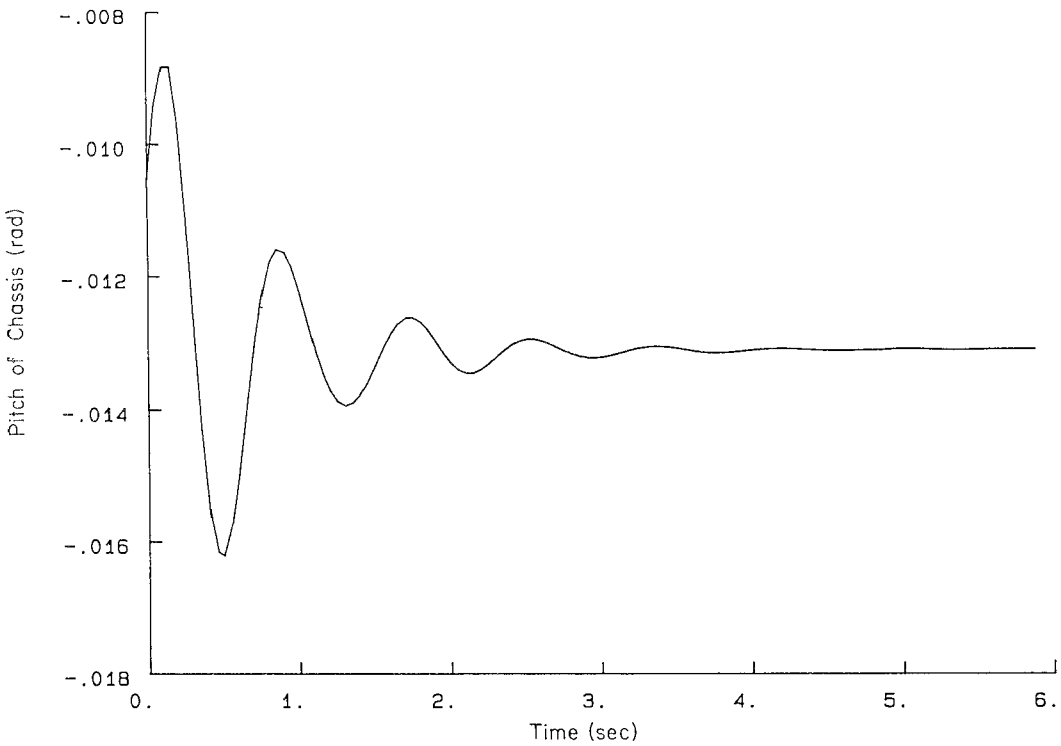

Figure 12.5.5 Vehicle equilibrium pitch (model 1).

TABLE 12.5.9 Equilibrium Configuration

Body \ GC		x	y	z	e_1	e_2	e_3
Chassis	①	0.0	0.0	0.5385	−0.0065	0.0	−0.0005
Wheel assembly	②	0.6014	1.1761	0.3449	−0.0022	−0.0065	−0.001
Wheel assembly	③	−0.5992	1.1772	0.3449	−0.0023	0.0065	−0.0002
Wheel assembly	④	0.5788	−1.2918	0.2617	−0.0075	−0.0003	−0.0005
Wheel assembly	⑤	−0.5812	−1.2907	0.2617	−0.0075	0.0003	−0.0005
Rack	⑥	0.0012	1.2625	0.1471	−0.0065	0.0	−0.0005
Stabilizing bar	⑦	0.001	1.0566	0.1983	0.0675	0.0	−0.0005
Stabilizing bar	⑧	−0.0013	−1.4097	0.3756	−0.0508	0.0	−0.0002

12.5.3 Steering Specification

In both models 1 and 2, a driving constraint is specified for translation of the rack, relative to the chassis, to simulate steering. Figure 12.5.6 shows three curves of rack position as functions of time. With curves 1 and 2, lane change maneuvers of the vehicle are expected. A circular path of the vehicle is expected with curve 3.

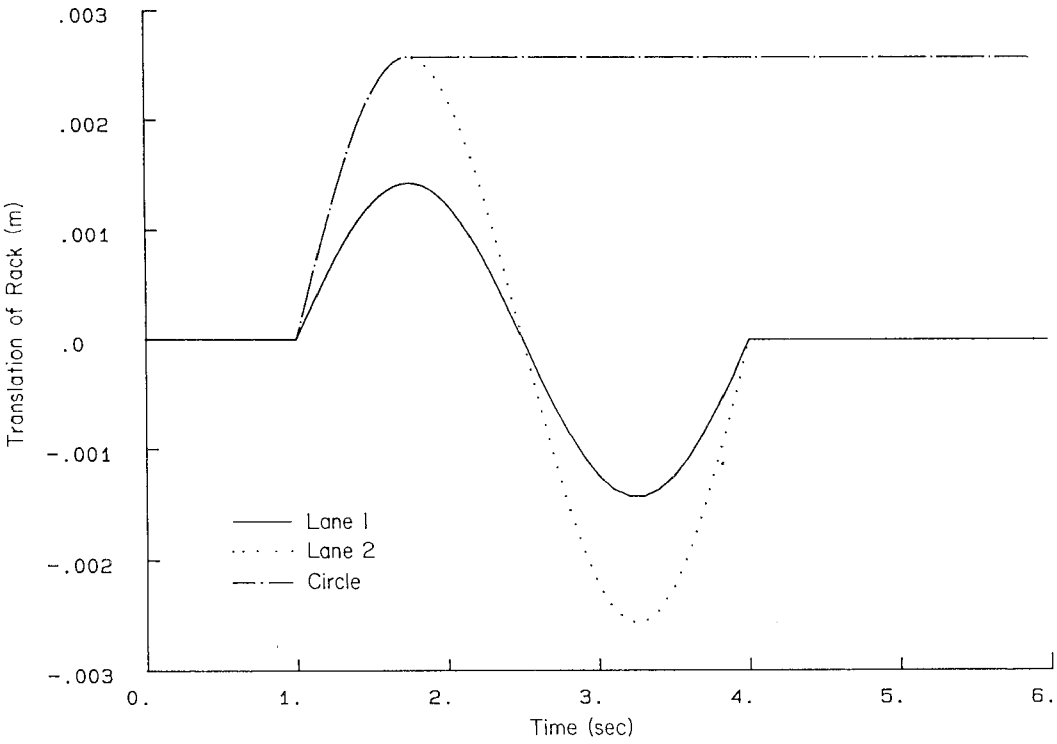

Figure 12.5.6 Rack driver for steering.

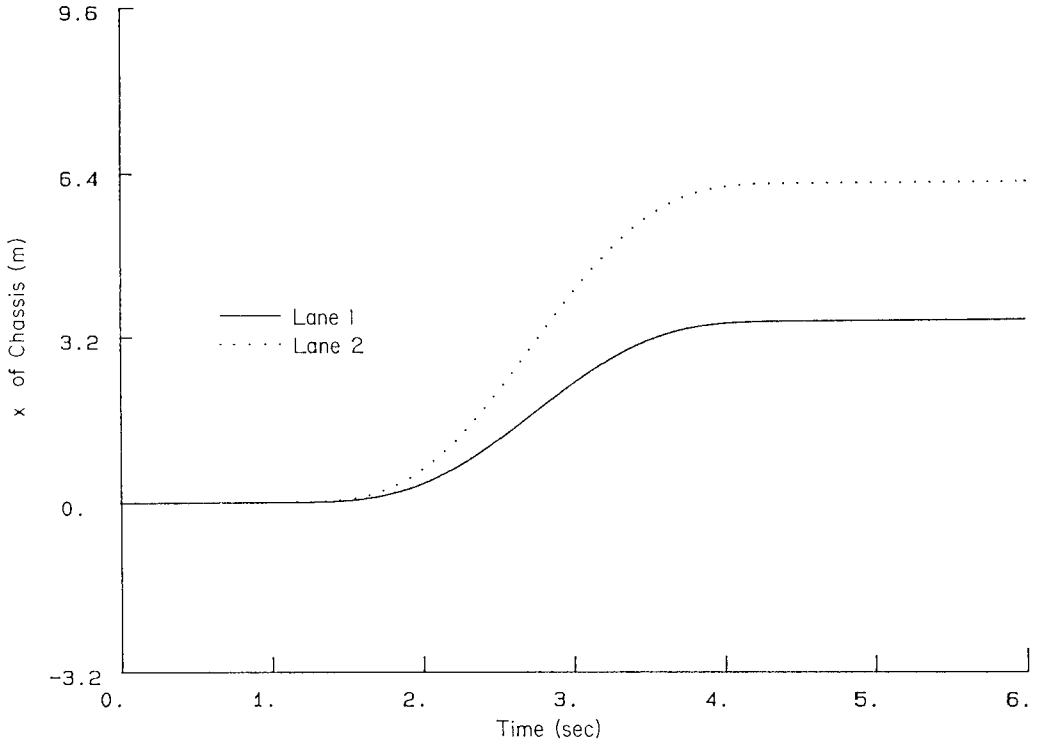

Figure 12.5.7 Lane–change position (model 1).

12.5.4 Dynamic Analysis

Lane Changes The dynamic response of the vehicle is analyzed by imposing an initial forward velocity $\dot{y}_0 = 55$ mph of the vehicle. Figures 12.5.7 and 12.5.8 show lateral positions and accelerations of model 1 for the two lane-change maneuvers. The pitch, roll, and yaw of the vehicle in lane change 2 are plotted in Fig. 12.5.9.

To see the stabilizing effect of roll-stabilizing bars, the dynamic response of model 2 in the lane-change maneuvers is obtained. Roll motions of the vehicle are compared in Fig. 12.5.10 for both models and with both lane-change drivers. The roll-stabilizer effect in model 2 is clearly observed.

Circular Path Three different initial speeds, $\dot{y}_0 = 20$, 40, and 55 mph, of the vehicle are used with steering input 3 of Fig. 12.5.6. The paths of the vehicle from these simulations are plotted in Fig. 12.5.11. For $\dot{y}_0 = 55$ mph, the maximum tire slip force occurs; that is, $F_{\text{lat}} = \mu F_{\text{ver}}$, until the speed of the vehicle substantially decreases due to large lateral slip. Figure 12.5.12 shows

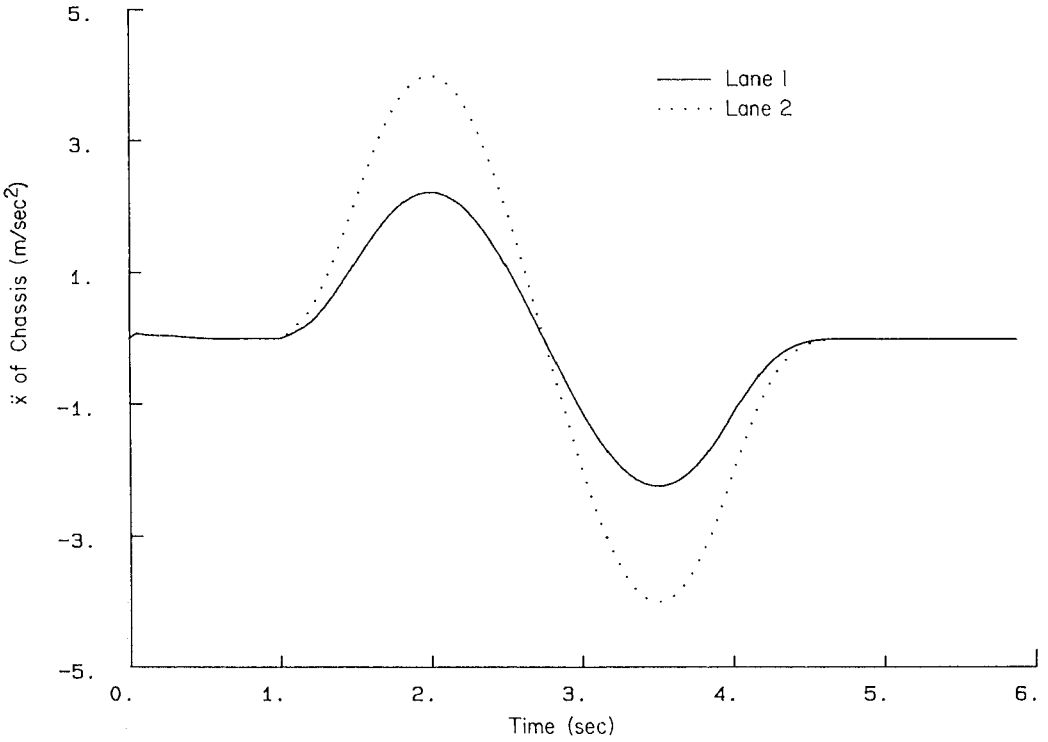

Figure 12.5.8 Lane-change acceleration (model 1).

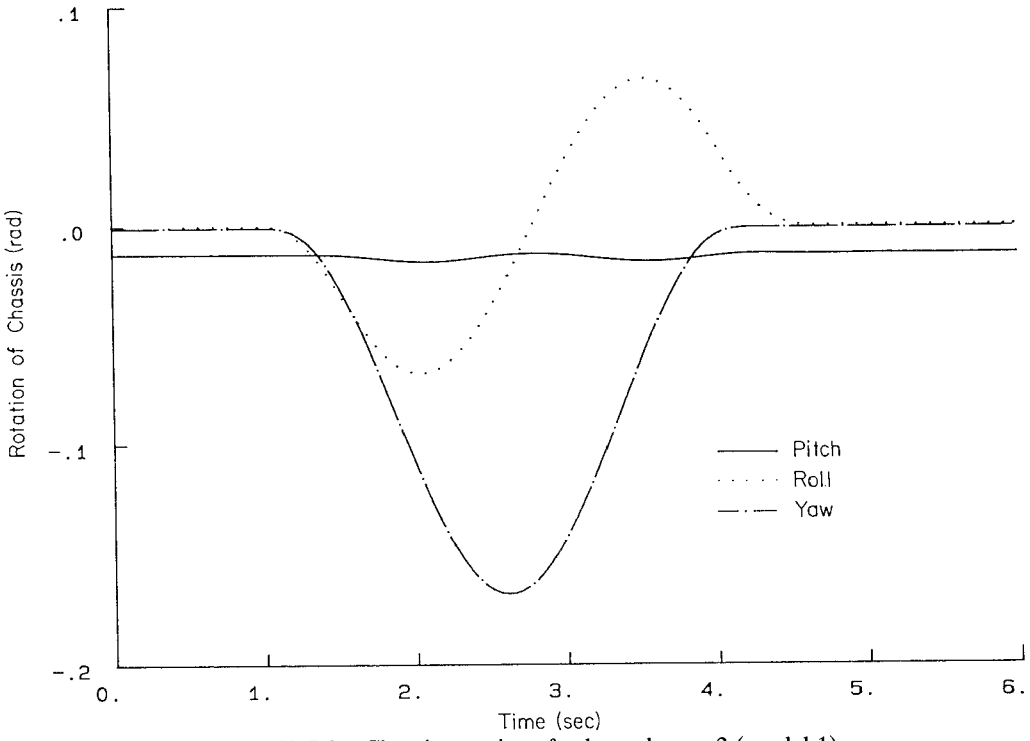

Figure 12.5.9 Chassis rotations for lane change 2 (model 1).

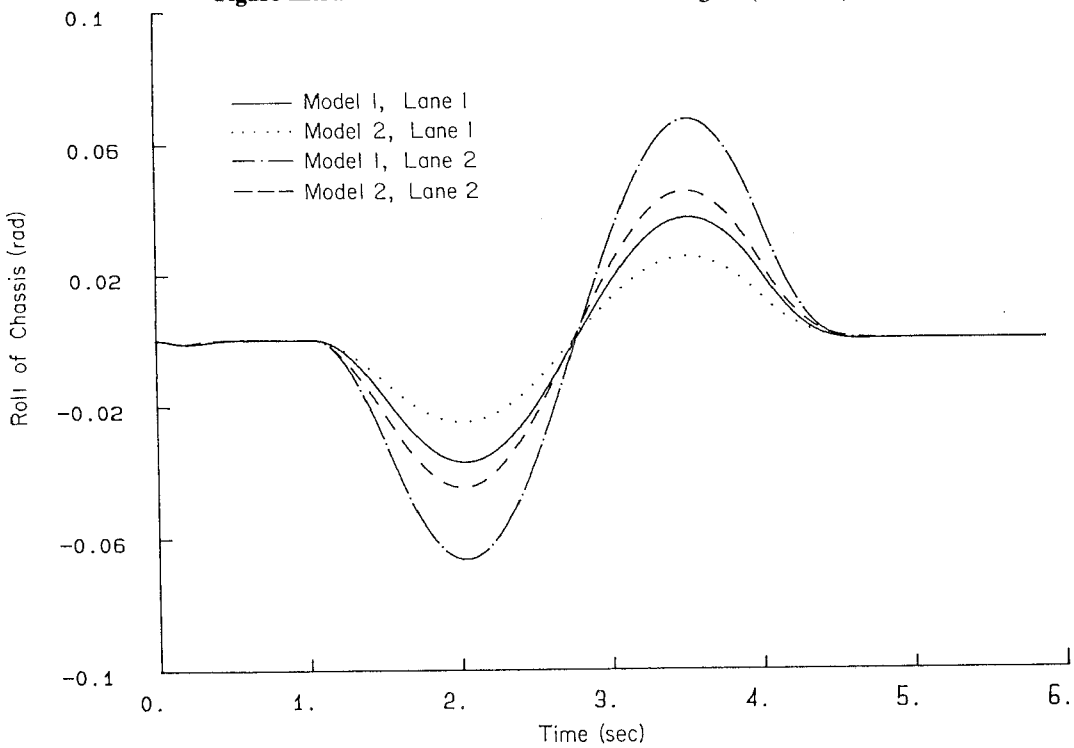

Figure 12.5.10 Chassis roll in lane changes.

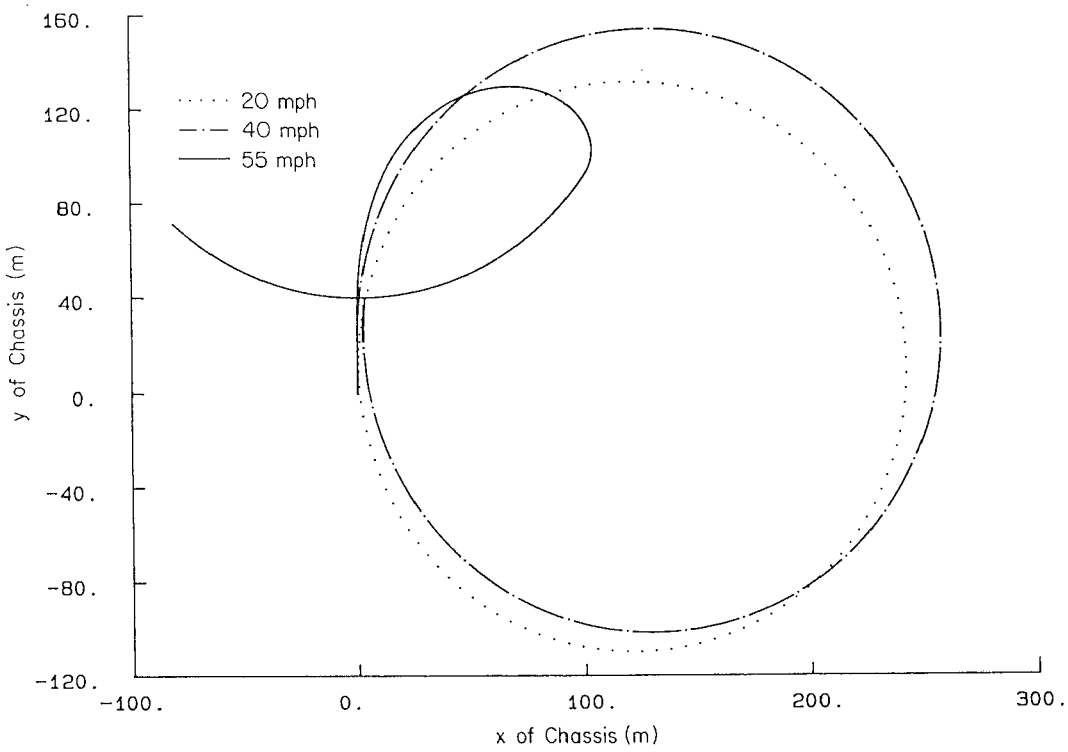

Figure 12.5.11 Chassis trajectory for circular steer input.

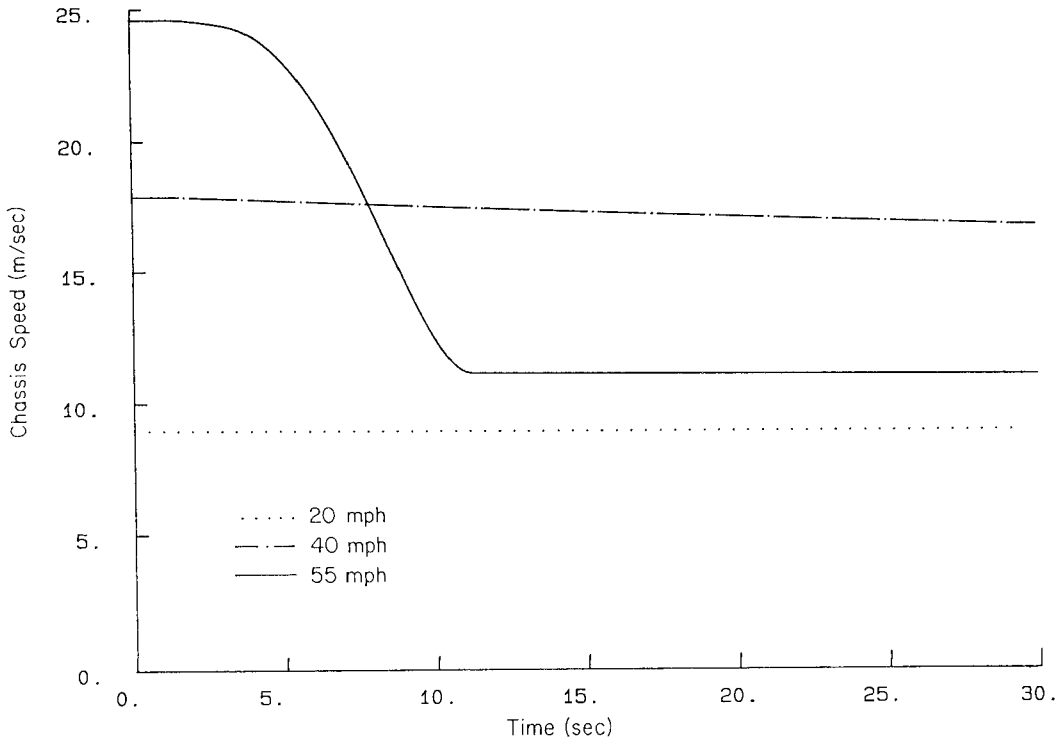

Figure 12.5.12 Chassis speed for cicular steer input.

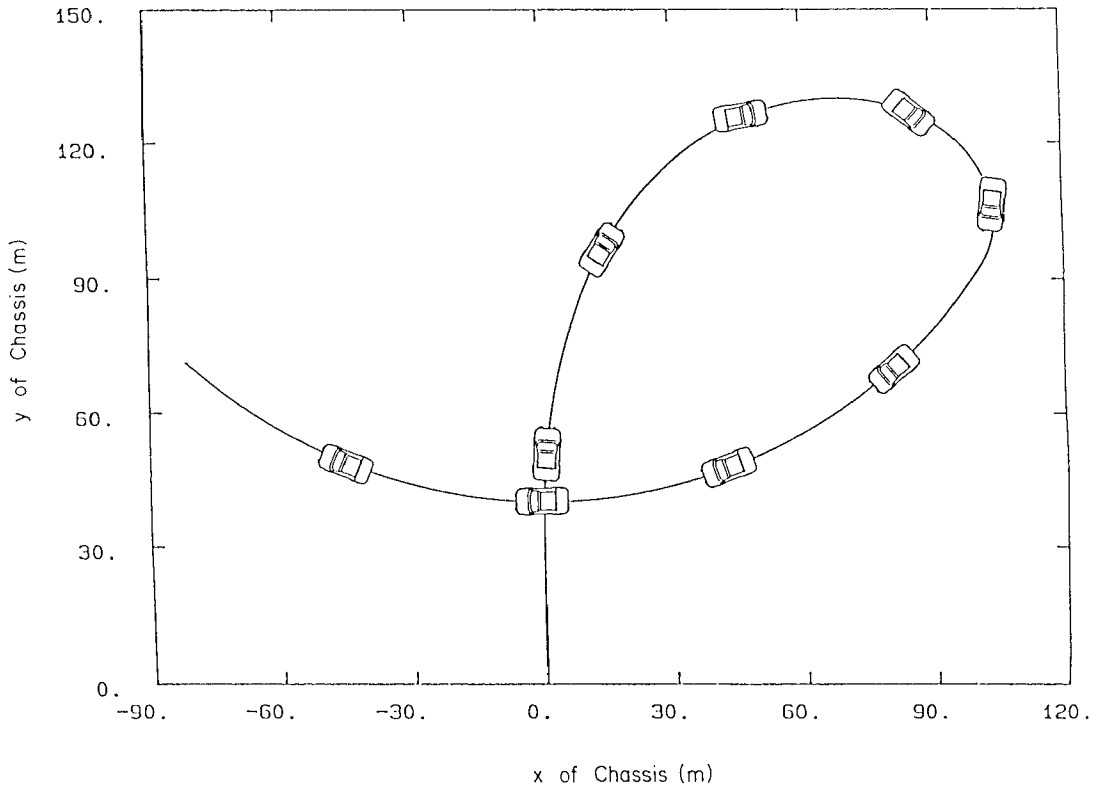

Figure 12.5.13 Vehicle orientation in circular steer maneuver (55 mph).

the speeds of the vehicle in the three different simulations. As expected, considerable speed loss (reduction in kinetic energy) occurs in the 55 mph case, since dissipative friction forces act while the vehicle is slipping laterally.

Figure 12.5.13 shows that the vehicle is not tangent to the path during the maximum slip period in the $\dot{y}_0 = 55$ mph simulation.

12.6 DYNAMIC ANALYSIS OF A GOVERNOR MECHANISM

12.6.1 Alternative Models

The governor mechanism shown in Fig. 12.6.1 is composed of five bodies, including ground (body 1). Bodies 2 to 5 are shaft, ball 1, ball 2, and collar, respectively. The arms attached to the balls are connected to the shaft by revolute joints whose axes are parallel, both perpendicular to the shaft. The

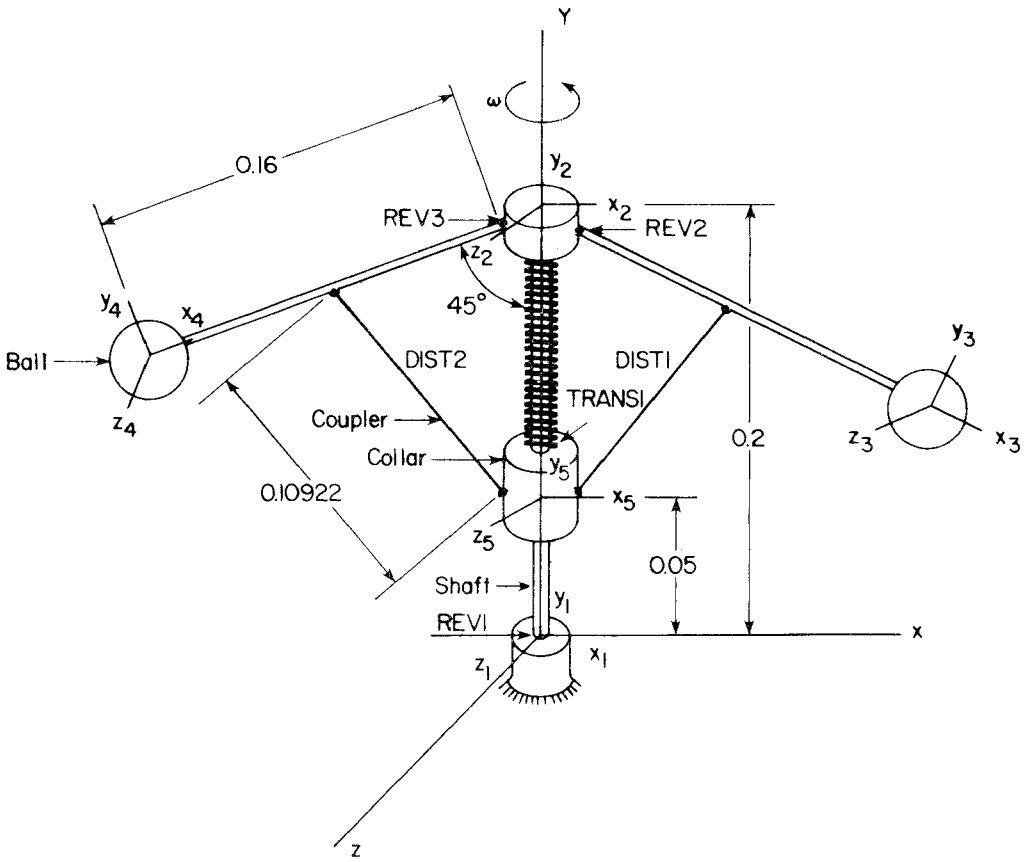

Figure 12.6.1 Governor mechanism.

collar is connected to the shaft by a translational joint. Couplers that connect the ball arms and collar are modeled as distance constraints. A TSDA element is attached between the shaft and collar. The inertia properties of the components of the system are defined in Table 12.6.1.

The intended function of the governor is to maintain a nearly constant

TABLE 12.6.1 Inertia Properties of Governor Mechanism

Body		Mass	$I_{x'}$	$I_{y'}$	$I_{z'}$	$I_{x'y'}$	$I_{y'z'}$	$I_{x'z'}$
Ground	①	1.0	1.0	1.0	1.0	0.0	0.0	0.0
Spindle	②	200.0	25.0	50.0	25.0	0.0	0.0	0.0
Ball 1	③	1.0	0.1	0.1	0.1	0.0	0.0	0.0
Ball 2	④	1.0	0.1	0.1	0.1	0.0	0.0	0.0
Collar	⑤	1.0	0.15	0.125	0.15	0.0	0.0	0.0

angular speed ω of the shaft under a varying resisting torque from the machine being driven. If the angular velocity of the shaft decreases, the balls drop and hence lower the collar. A linkage attached to the collar then opens the fuel feed to the engine, which generates an increased torque and leads to a speed-up of the shaft. As a result, the balls rise toward their nominal position as the shaft angular velocity approaches the desired value.

The elements of the kinematic model are as follows:

Bodies	
Five bodies	$nc = 35$
Constraints	
Distance constraint: DIST1	1
Distance constraint: DIST2	1
Revolute joint: REV1	5
Revolute joint: REV2	5
Revolute joint: REV3	5
Translational joint: TRANS1	5
Ground constraint	6
Normalization constraint	5
Euler parameter	
	$nh = 33$
DOF = 35 − 33 = 2.	

Data for the distance constraints, revolute joints, and translational joint are tabulated in Tables 12.6.2 to 12.6.4. Data for the TSDA element are given in Table 12.6.5. Three different models (1, 2, and 3) are distinguished, with spring constants $k = 1000$, 2000, and 3000 N/m, respectively.

TABLE 12.6.2 Data for Distance Constraints

DIST1

Body \ Point	P			Q			R		
	x'	y'	z'	x'	y'	z'	x'	y'	z'
Ball 1 ③	−0.08	0.0	0.0	−0.08	0.0	1.0	1.08	0.0	0.0
Collar ⑤	0.0	0.0	0.0	0.0	0.0	1.0	1.0	0.0	0.0

Distance = 0.10922

DIST2

Body \ Point	P			Q			R		
	x'	y'	z'	x'	y'	z'	x'	y'	z
Ball 2 ④	0.08	0.0	0.0	0.08	0.0	1.0	1.08	0.0	0.0
Collar ⑤	0.0	0.0	0.0	0.0	0.0	1.0	1.0	0.0	0.0

Distance = 0.10922

TABLE 12.6.3 Data for Revolute Joints

REV1

Body \ Point	P			Q			R		
	x'	y'	z'	x'	y'	z'	x'	y'	z'
Ground ①	0.0	0.0	0.0	0.0	1.0	0.0	0.0	0.0	1.0
Spindle ②	0.0	−0.2	0.0	0.0	−1.2	0.0	0.0	−0.2	1.0

REV2

Body \ Point	P			Q			R		
	x'	y'	z'	x'	y'	z'	x'	y'	z'
Spindle ②	0.0	0.0	0.0	0.0	0.0	1.0	1.0	0.0	0.0
Ball 1 ③	−0.16	0.0	0.0	−0.16	0.0	1.0	1.0	0.0	0.0

REV3

Body \ Point	P			Q			R		
	x'	y'	z'	x'	y'	z'	x'	y'	z'
Spindle ②	0.0	0.0	0.0	0.0	0.0	1.0	1.0	0.0	0.0
Ball 2 ④	0.16	0.0	0.0	0.16	0.0	1.0	1.0	0.0	0.0

TABLE 12.6.4 Data for Translational Joint

Body \ Point	P			Q			R		
	x'	y'	z'	x'	y'	z'	x'	y'	z'
Spindle ②	0.0	0.0	0.0	0.0	1.0	0.0	0.0	0.0	1.0
Collar ⑤	0.0	0.0	0.0	0.0	1.0	0.0	0.0	0.0	1.0

TABLE 12.6.5 Data for Translational Spring–Damper–Actuator

Body \ Point	P			Q			R		
	x'	y'	z'	x'	y'	z'	x'	y'	z'
Spindle ②	0.0	0.0	0.0	0.0	0.0	1.0	1.0	0.0	0.0
Collar ⑤	0.0	0.0	0.0	0.0	0.0	1.0	1.0	0.0	0.0

Spring constant, $k = 1000, 2000, 3000$ N/m

Damping rate, $c = 30$ kg/s

Free length of spring, $L_0 = 0.15$ m

12.6.2 Steady-State Analysis

Based on the configuration of Fig. 12.6.1, steady-state motion is determined by selecting the desired angular speed ω of the spindle. Using dynamic force balancing and $\omega = 11.0174$ rad/s, at a slope of 45° of the ball arms, the collar is to be stationary. Table 12.6.6 defines the steady-state configuration of the system.

TABLE 12.6.6 Data for Steady-State Configuration

Body		x	y	z	e_0	e_1	e_2	e_3
Ground	①	0.0	0.0	0.0	1.0	0.0	0.0	0.0
Spindle	②	0.0	0.2	0.0	1.0	0.0	0.0	0.0
Ball 1	③	0.11314	0.08686	0.0	0.9239	0.0	0.0	0.3827
Ball 2	④	−0.11314	0.08686	0.0	0.9239	0.0	0.0	0.3827
Collar	⑤	0.0	0.05	0.0	1.0	0.0	0.0	0.0

12.6.3 External Torque

An external torque T_e due to the load driven by the shaft is applied to the spindle, as shown in Fig. 12.6.2. To compensate for this torque, which tends to reduce shaft speed, the torque T_s applied to the spindle by the engine as a result of fuel fed by a collar height variation $\Delta\ell$ is modeled as

$$T_s = C \times \Delta\ell \tag{12.6.1}$$

where C is the torque generated due to fuel fed to the engine by a unit $\Delta\ell$, which is spring deformation (vertical movement of collar). Three different values $C = 7500$, 12,500, and 17,500, corresponding to increasing engine power, are used to study the system dynamic response.

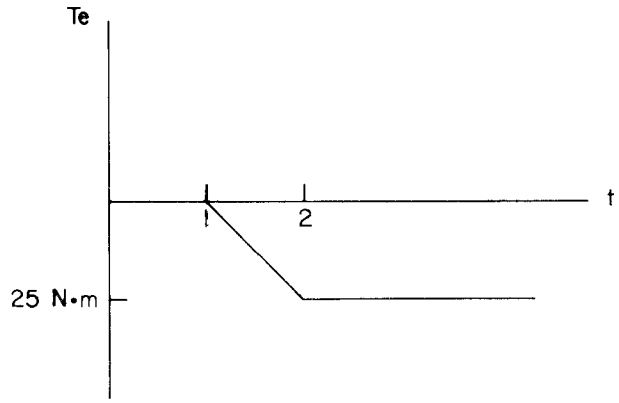

Figure 12.6.2 External torque on spindle.

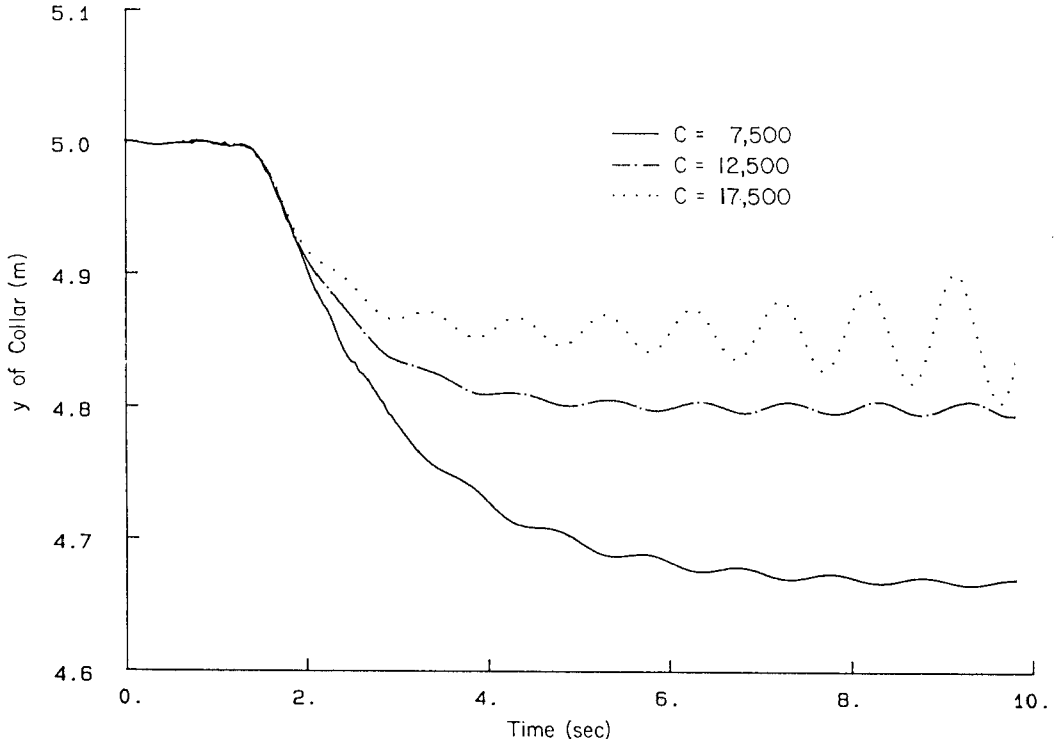

Figure 12.6.5 y of collar versus time ($k = 1000$).

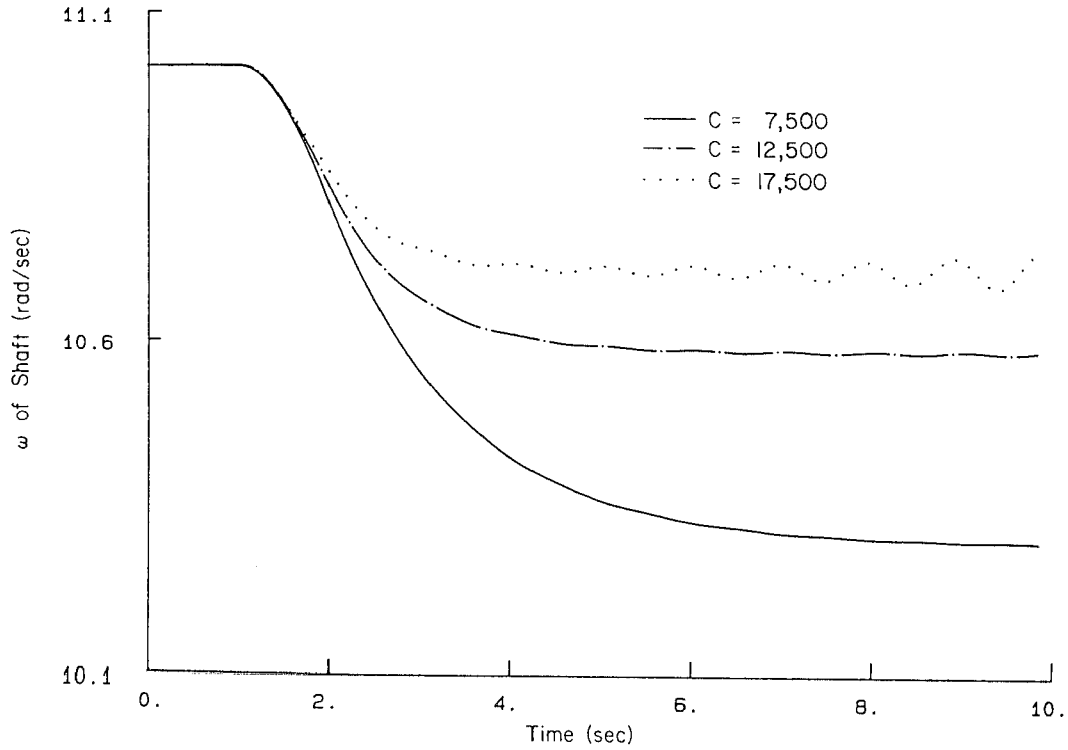

Figure 12.6.6 ω of shaft versus time ($k = 1000$).

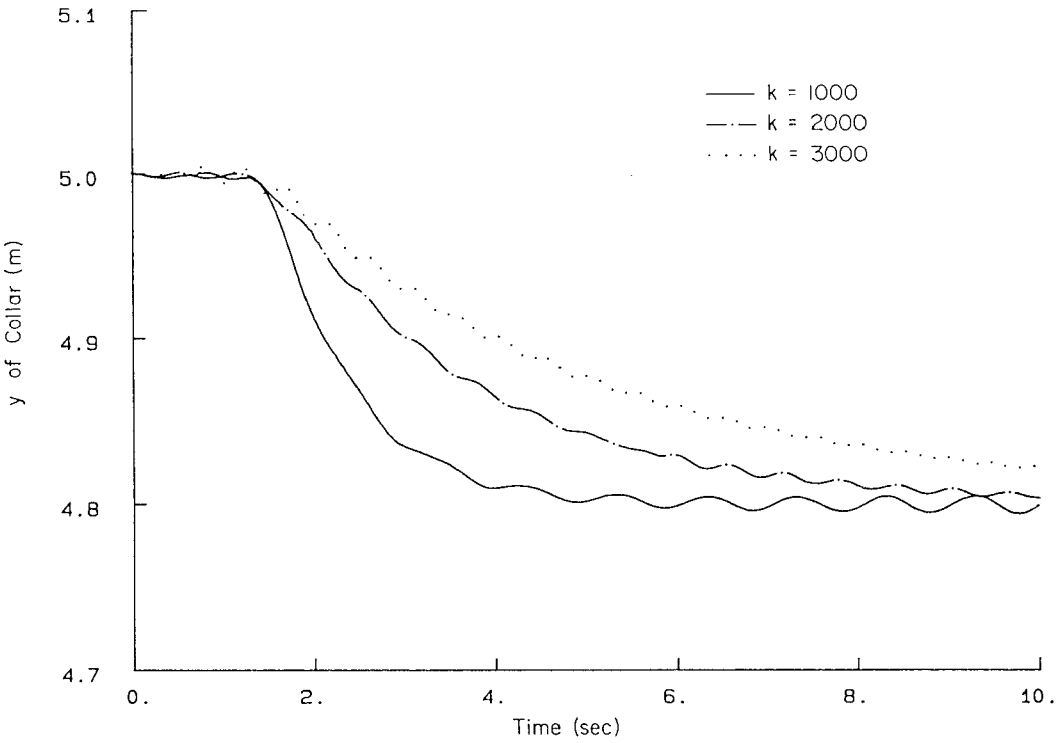

Figure 12.6.3 y of collar versus time ($C = 12{,}500$).

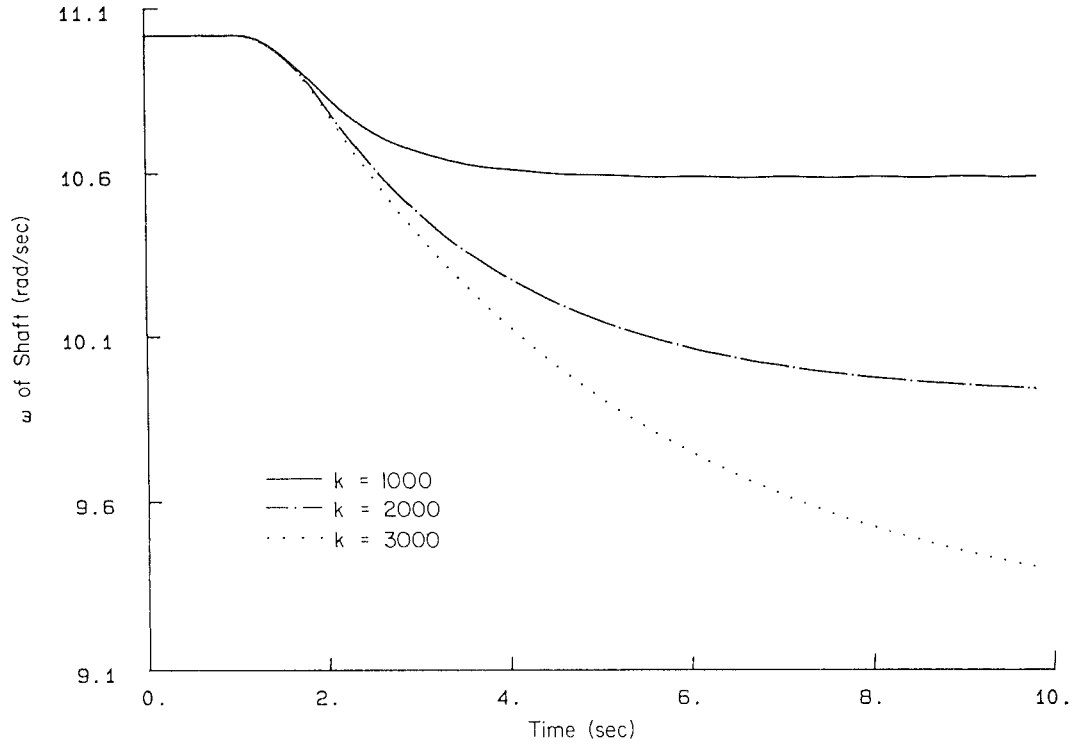

Figure 12.6.4 ω of shaft versus time ($C = 12{,}500$).

12.6.4 Dynamic Analysis

Starting with the given steady-state configuration and $C = 12{,}500$, dynamic simulations are performed for three different values of the spring rate k. Figures 12.6.3 and 12.6.4 show variations in the vertical position of the collar and angular speed of the shaft. Note that the stiffer the spring, the longer the transition time from the initial steady state to another steady state.

Dynamic responses are plotted in Figs. 12.6.5 and 12.6.6 for different torque feedback rates, with $k = 1000$. As the feedback rate becomes larger (more powerful engine), the system may become unstable.

PROBLEMS

DADS Projects

12.1 Using the three body model of DADS Project 10.1, repeat the dynamic analysis of the spatial slider–crank mechanism presented in Section 12.2. Analyze the differences in required driving torque and dynamic response from those presented in Sections 12.2.2 and 12.2.3, due to the elimination of connecting rod inertias.

12.2 Using the data in Section 12.4 and the following inertial properties of each connecting rod, carry out a dynamic analysis of the fifteen-body air compressor model of DADS Project 10.2

Mass	$I_{x'x'}$	$I_{y'y'}$	$I_{z'z'}$	$I_{x'y'}$	$I_{y'z'}$	$I_{z'x'}$
0.5	0.04	0.04	0.001	0.0	0.0	0.0

where the center of mass of the connecting rod is at its midpoint and its z' axis is along the rod.

Evaluate the differences in driving torque, reaction forces, and dynamic response from those presented in Section 12.4, due to the inertias of the connecting rods.

References

1. Beyer, R., *The Kinematic Synthesis of Mechanisms,* McGraw-Hill, New York, 1963.
2. Hirschhorn, J., *Kinematics and Dynamics of Plane Mechanisms,* McGraw-Hill, New York, 1962.
3. Paul, B., *Kinematics and Dynamics of Planar Machinery,* Prentice-Hall, Englewood Cliffs, N.J., 1979.
4. Wittenburg, J., *Dynamics of Systems of Rigid Bodies,* Teubner, Stuttgart, 1977.
5. Soni, A. H., *Mechanism Synthesis and Analysis,* McGraw-Hill, New York, 1974.
6. Suh, C. H., and Radcliffe, C. W., *Kinematics and Mechanisms Design,* Wiley, New York, 1978.
7. Greenwood, D. T., *Principles of Dynamics,* 2nd ed., Prentice-Hall, Englewood Cliffs, N.J., 1988.
8. Kane, T. R., and Levinson, D. A., *Dynamics: Theory and Applications,* McGraw-Hill, New York, 1985.
9. Goldstein, H., *Classical Mechanics,* 2nd ed., Addison-Wesley, Reading, Mass., 1980.
10. Noble, B., and Hussain, M. A., "Applications of MACSYMA to Calculations in Dynamics," *Computer Aided Analysis and Optimization of Mechanical System Dynamics* (ed. E. J. Haug), Springer-Verlag, Heidelberg, 1984.
11. Zienkiewiez, O., *The Finite Element Method,* McGraw-Hill, New York, 1977.
12. Gallagher, R. H., *Finite Element Analysis: Fundamentals,* Prentice-Hall, Englewood Cliffs, N.J., 1975.
13. Chua, L. O., and Lin, P.-M., *Computer Aided Analysis of Electronic Circuits,* Prentice-Hall, Englewood Cliffs, N.J., 1975.
14. Calahan, D. A., *Computer Aided Network Design,* McGraw-Hill, New York, 1972.
15. Paul, B., and Krajcinovic, D., "Computer Analysis of Machines with Planar Motion—Part I: Kinematics; Part II: Dynamics," *Journal of Applied Mechanics,* Vol. 37, pp. 697–712, 1970.
16. Chace, M. A., and Smith, D. A., "DAMN—A Digital Computer Program for the Dynamic Analysis of Generalized Mechanical Systems," SAE paper 710244, January 1971.
17. Sheth, P. N., and Uicker, J. J., Jr., "IMP (Integrated Mechanisms Program), A Computer Aided Design Analysis System for Mechanisms and Linkages," *Journal of Engineering for Industry,* Vol. 94, pp. 454–464, 1972.
18. Orlandea, N., Chace, M. A., and Calahan, D. A., "A Sparsity-Oriented Approach to the Dynamic Analysis and Design of Mechanical Systems, Parts I and II," *Journal of Engineering for Industry,* Vol. 99, pp. 773–784, 1977.

19. Wehage, R. A., and Haug, E. J., "Generalized Coordinate Partitioning for Dimension Reduction in Analysis of Constrained Dynamic Systems," *Journal of Mechanical Design,* Vol. 104, No. 1, pp. 247–255, 1982.
20. Chung, I. S., and others, *Dynamic Analysis of Three Dimensional Constrained Mechanical Systems Using Euler Parameters,* Technical Report No. 81-11, Center for Computer Aided Design, College of Engineering, University of Iowa, Iowa City, Iowa, October, 1981.
21. Davis, H. F., *Introduction to Vector Analysis,* 4th ed., Allyn & Bacon, Newton, Mass., 1979.
22. Strang, G., *Linear Algebra and Its Applications,* 2nd ed., Academic Press, New York 1980.
23. Erdman, A. G., and Sandor, G. N., *Advanced Mechanism Design: Analysis and Synthesis,* Vols. I and II, Prentice-Hall, Englewood Cliffs, N.J., 1984.
24. de Boor, C., *A Practical Guide to Splines,* Springer-Verlag, New York, 1978.
25. Goffman, C., *Calculus of Several Variables,* Harper & Row, New York, 1965.
26. Corwin, L. J., and Szczarba, R. H., *Multivariable Calculus,* Marcel Dekker, New York, 1982.
27. *DADS User's Manual,* Computer Aided Design Software Incorporated, P.O. Box 203, Oakdale, Iowa, 52319.
28. Haug, E. J., and Arora, J. S., *Applied Optimal Design,* Wiley-Interscience, New York, 1979.
29. Fletcher, R., and Powell, M. J. D., "A Rapidly Convergent Descent Method for Minimization," *Computer Journal,* Vol. 6, pp. 163–180, 1963.
30. Hildebrand, F. B., *Introduction to Numerical Analysis,* McGraw-Hill, New York, 1956.
31. Atkinson, K. E., *An Introduction to Numerical Analysis,* Wiley, New York, 1978.
32. Truesdell, C. A., *Essays in the History of Mechanics,* Springer-Verlag, New York, 1968.
33. Fiacco, A. V., and McCormick, G. P., *Nonlinear Programming: Sequential Unconstrained Minimization Techniques,* Wiley, New York, 1968.
34. Langhaar, H. L., *Energy Methods in Applied Mechanics,* Wiley, New York, 1962.
35. Haug, E. J., *Intermediate Dynamics,* Allyn & Bacon, Newton, Mass., 1989.
36. Shampine, L. F., and Gordon, M. K., *Computer Solution of Ordinary Differential Equations: The Initial Value Problem,* Freeman, San Francisco, 1975.
37. Gear, C. W., *Numerical Initial Value Problems in Ordinary Differential Equations,* Prentice-Hall, Englewood Cliffs, N.J., 1971.
38. Enright, W. H., "Numerical Methods for Systems of Initial Value Problems—The State of the Art," *Computer Aided Analysis and Optimization of Mechanical System Dynamics* (ed. E. J. Haug), Springer-Verlag, Heidelberg, 1984, pp. 309–322.
39. Petzold, L. D., "Differential/Algebraic Equations Are Not ODE's," *SIAM Journal of Scientific and Statistical Computing,* Vol. 3, No. 3, pp. 367–384, 1982.
40. Baumgarte, J., "Stabilization of Constraints and Integrals of Motion," *Computer Methods in Applied Mechanics and Engineering,* Vol. 1, pp. 1–16, 1972.
41. Mani, N. K., and Haug, E. J., "Singular Value Decomposition for Dynamic System Design Sensitivity Analysis," *Engineering with Computers,* Vol. 1, pp. 103–109, 1985.
42. Park, T., "A Hybrid Constraint Stabilization—Generalized Coordinate Partitioning Method for Machine Dynamics," *Journal of Mechanisms, Transmissions, and Automation in Design,* Vol. 108, No. 2, 1986, pp. 211–216.

43. Lotstedt, P., and Petzold, R., "Numerical Solution of Nonlinear Differential Equations with Algebraic Constraints," Sandia Report SAND 83-8877, Sandia National Laboratories, Albuquerque, N.M. 87185, 1983.
44. Coddington, E. A., and Levinson, N., *Theory of Ordinary Differential Equations,* McGraw-Hill, New York, 1955.
45. Park, T., Haug, E. J., and Yim H. J., "Automated Mechanism and Machine Theory, Kinematic Feasibility Evaluation and Analysis of Mechanical Systems," *Mechanism and Machine Theory,* 1988.
46. Duff, I. S., Erisman, A. M., and Reid, J. K., *Direct Methods for Sparse Matrices,* Oxford University Press, New York, 1986.
47. Duff, I. S., *MA28-A Set of Fortran Subroutines for Sparse Unsymmetric Linear Equations,* AIRE Harwell, Didcot, Oxon, U.K., 1977.
48. Kwon, O. K., and Haug, E. J., *An Index One Formulation of Differential–Algebraic Equations for Mechanical System Dynamics,* Center for Computer Aided Design, Technical Report 87-9, University of Iowa, Iowa City, Iowa, 1987.